Thin–Walled Structures 230 (2026) 115252

Contents lists available at ScienceDirect

Thin-Walled Structures

journal homepage: www.elsevier.com/locate/tws

Full length article

Enhanced energy absorption in re-entrant honeycombs via elliptical double-arrow hybrid design

Wenpeng Xu [a], Dongxia Wang [a], Jinglong Zhang [a], Jiahe Hu [a], Hao Xu [b], Liuchao Jin [c], Haitao Ye [c], Haisen Zhao [b], Wei-Hsin Liao [c,d,*]

[a] School of Computer Science and Technology, Henan Polytechnic University, Jiaozuo, 454003, China
[b] School of Computer Science and Technology, Shandong University, Qingdao, 266237, China
[c] Department of Mechanical and Automation Engineering, The Chinese University of Hong Kong, Hong Kong, China
[d] Institute of Intelligent Design and Manufacturing, The Chinese University of Hong Kong, Hong Kong, China

ARTICLE INFO

Dataset link: https://doi.org/10.6084/m9.figshare.31725139

Keywords:
Honeycomb structures
Energy absorption
Mechanical metamaterials
Finite element analysis
Impact protection

ABSTRACT

Honeycomb metastructures are widely applied due to their lightweight and high specific strength characteristics. However, their energy absorption and load-bearing capacities remain limited. Hybrid designs integrating multiple structural forms have shown potential for enhanced mechanical performance. This paper presents a novel hybrid re-entrant honeycomb metastructure, termed the re-entrant elliptical double-arrow hybrid honeycomb (REDA). The design replaces the horizontal walls of the re-entrant honeycomb (RH) with double-arrow units and incorporates thin-walled ellipses at the concave corners and horizontal midpoints to improve structural performance. To validate its effectiveness, the energy absorption performance of the proposed REDA is evaluated through key indicators, and a theoretical model of the plateau stress is derived to support its mechanical interpretation. Results show that the REDA exhibits markedly improved energy absorption, with specific energy absorption up to five times higher than that of the RH structure under the same wall thickness conditions, and increasing by 202.07%, 138.30%, 67.16%, and 52.14% compared to the re-entrant hollow-circle honeycomb (RHC), RH, star-shaped re-entrant honeycomb (SRH), and elliptical annular re-entrant honeycomb structure (EARE), respectively, at the same relative density. A mini truck impact test further demonstrates the reliable mechanical response of the proposed structure under impact loading, with the insertion depth reduced by approximately 45.5% and 57.1% compared to the RH1 structure under low and high mass conditions, respectively, and by 35.7% and 45.1% compared to the RH2 structure, highlighting its potential for applications in vehicle protection, vibration mitigation, and personal safety equipment.

1. Introduction

Honeycomb metastructures are widely used in aerospace [1], automotive engineering [2,3], medical devices [4], load-bearing equipment [5,6], and energy-absorbing systems [7–9], owing to their lightweight nature [10,11], high porosity, and excellent specific energy absorption [12]. Among various configurations, the re-entrant honeycomb (RH) structure, characterized by its negative Poisson's ratio (NPR) [13,14], offers unique mechanical advantages such as enhanced indentation resistance [15,16], improved shear modulus [17,18], superior fracture toughness [19], as well as excellent impact resistance [20,21], and specific energy absorption [22,23]. The inward-facing geometry of RH cells promotes energy absorption under compression, but conventional RH structures cannot simultaneously ensure high stiffness, deformation stability, and imperfection tolerance, limiting their practical application.

To overcome the limitations of conventional honeycomb structures, researchers have attempted to employ data-driven methods to optimize cell geometries and predict energy absorption performance [24–28]. However, machine learning depends on large datasets and has limited generalization capability. In contrast, hybrid honeycomb designs combine multiple cell geometries to achieve synergistic energy absorption, stiffness, and impact resistance. Geometric customization further expands the design space and enhances mechanical tunability, offering a promising route for advanced structural performance.

Recent work on hybrid and re-entrant honeycombs has focused on regulating deformation modes to balance structural stability and energy absorption. By introducing innovative unit geometries such as narrow-rib cells [29], diamond-shaped cells [30–32], concentric-wall designs [33], concave-arc cells [34], inclined-wall configurations [35],

* Corresponding author.
E-mail address: whliao@cuhk.edu.hk (W.-H. Liao).

https://doi.org/10.1016/j.tws.2026.115252
Received 4 April 2026; Received in revised form 20 May 2026; Accepted 5 June 2026
Available online 11 June 2026

and curved-wall designs [36], researchers have achieved better control over deformation modes, thereby enhancing structural stiffness and energy absorption capacity. Zhang et al. [37] enhanced stiffness and auxetic behavior through a wedge-shaped configuration. Tatler et al. [38] boosted energy absorption performance in their modified re-entrant cell structure by embedding circular walls. Zhu et al. [39] proposed an elliptical-arc re-entrant honeycomb (EARE) to enhance stiffness and alleviate the inherent stiffness-deformability trade-off in traditional designs. The introduction of the elliptical annular structure leads to a distinctive deformation mode characterized by staged collapse behavior and enhanced longitudinal support during compression. For instance, Chen and Wang [40] enhanced the specific Young's modulus and shear modulus through re-entrant hollow-circular honeycomb (RHC) designs, The introduction of hollow-circular junctions modifies the deformation mode by redistributing local stress and improving in-plane stiffness. Li et al. [41] proposed a star-rhombic honeycomb (SRH) that hybridizes rhombic and star-shaped cells, where the added diagonal struts enhance both load-bearing capacity and energy absorption while maintaining auxetic properties. While Mo et al. [42] introduced a hierarchical auxetic star-shaped honeycomb, in which internal supports significantly enhance energy absorption and deformation stability. Qi et al. [43–45] proposed a re-entrant circular honeycomb with double-arc walls, which exhibits an X-shaped deformation mode under compression and enhanced energy absorption due to the formation of additional plastic hinges. Zhou et al. [46] developed the reinforced composite-wall honeycomb structure, which enhanced compressive strength and impact stability through layered design. Alomarah et al. [47,48] proposed a butterfly-shaped auxetic metamaterial (BSAM) and its 3D variants, which achieve two distinctive plateau regimes by sequentially collapsing weaker and stronger layers within the unit cell, thereby enhancing energy absorption. These studies demonstrate that tailored cell geometries can effectively improve load-bearing and energy absorption performance. However, existing designs often exhibit insufficient stiffness and unstable deformation during compression, which may lead to non-uniform collapse, uneven stress redistribution, and fluctuating stress responses. Recent studies have shown that the energy absorption capability of cellular structures is strongly influenced not only by stiffness and relative density, but also by deformation stability, collapse coordination, and the evolution of load-transfer paths during compression. Therefore, regulating the deformation mode and promoting progressive energy dissipation have become important design strategies for improving the mechanical performance of advanced auxetic and re-entrant honeycomb metamaterials.

To clarify these limitations, a comparative analysis was conducted among SRH, RH, RHC, and EARE unit cells. The SRH structure introduces star-shaped internal reinforcements to improve the deformation behavior and load-bearing performance of the cellular structure. The additional internal members help distribute deformation more uniformly during compression and enhance the initial structural stiffness. However, its plateau stress and energy absorption capacity remain relatively low, indicating that the star-shaped reinforcement provides only limited improvement in load transfer and plastic energy dissipation [41]. When compressed along the in-plane directions, the RH structure tends to exhibit non-uniform deformation, often accompanied by global buckling, indicating that its deformation behavior is not inherently stable [47,49]. In addition, due to the absence of internal support in its re-entrant core, the structure suffers from low stiffness and underutilized material regions near the boundary connections. The lack of internal support also results in relatively simple load-transfer paths and limited plastic dissipation zones, which may lead to early local instability during compression. Although RHC and EARE introduce partial reinforcements, deformation instability still occurs during compression, and the outermost cell connections remain inefficiently utilized. Specifically, RHC mainly enhances the boundary regions through circular reinforcements, whereas its contribution to coordinated internal load transfer and distributed plastic energy dissipation across the unit cell remains limited [40]. In particular, EARE shows a distinct two-stage deformation pattern, where energy absorption is relatively low in the initial stage and increases significantly only after the circular component becomes fully engaged, which also leads to a pronounced stress rise [37].

To overcome these limitations, this study proposes the REDA configuration, as illustrated in Fig. 1a, in which thin-walled elliptical elements and double-arrow units are integrated into the re-entrant framework. The elliptical elements are introduced at the concave corners and horizontal midpoints, where they constrain the inward deformation of the re-entrant walls, suppress excessive local collapse in the middle region, and redistribute the applied load within the unit cell. During compression, part of the load is transferred through the elliptical components, resulting in a more distributed stress field and improved deformation coordination among adjacent unit cells. Owing to their continuously curved geometry, the elliptical segments also promote progressive bending deformation and more stable energy dissipation during compression. Meanwhile, the double-arrow units replace the conventional horizontal walls, introducing additional inclined load-transfer paths and increasing the number of potential plastic dissipation regions, which helps prolong the plastic plateau stage and promote coordinated deformation. This design enhances structural stiffness, promotes coordinated deformation among adjacent cells, and improves overall material utilization. Therefore, unlike SRH structures with limited star-shaped reinforcement effects, RH structures with no internal support, and RHC structures with mainly boundary reinforcement, REDA combines internal reinforcement, load-path reconstruction, and cooperative energy dissipation. As illustrated in Figs. 1b–1d, the REDA structure exhibits a more uniform and stable collapse mode, accompanied by higher initial stiffness, a more stable plateau stress, and a steadier energy absorption evolution compared with SRH, RH, RHC, and EARE, thereby validating the effectiveness of the proposed design strategy. These results also highlight the practical applicability of the proposed REDA configuration. As illustrated in Fig. 1e, the improved stiffness, deformation stability, and energy absorption capacity suggest strong potential for applications in vehicle impact protection, structural vibration mitigation, and personal protective equipment.

The remainder of this paper is organized as follows. Section 2 presents the structural design of the REDA configuration, the experimental details, finite element modeling, performance indicators, and theoretical modeling of the plateau stress. Section 3 discusses the experimental validation, comparison with existing honeycomb structures, and parametric analysis. Section 4 presents an application demonstration using a mini truck model to evaluate the response of the proposed structure under low-velocity impact loading. Section 5 summarizes the main conclusions and outlines future research directions.

2. Materials and methods

2.1. Structural design of REDA

Under in-plane compression, honeycomb energy absorption depends on deformation coordination, effective load paths, and plastic hinge formation. Conventional re-entrant honeycombs suffer from local buckling, stress concentration, and limited energy absorption. To overcome these limitations, this study proposes a novel re-entrant elliptical double-arrow hybrid honeycomb, enhancing the conventional RH design with elliptical and double-arrow connecting units to improve structural stability and energy absorption.

As shown in Fig. 1a, the conventional RH structure comprises inclined walls of length l, horizontal walls of length w, horizontal connectors of length $\frac{\sqrt{3}}{2}l$, and an angle α between inclined and horizontal walls. The REDA structure introduces two modifications: the horizontal connectors are replaced with double-arrow units, defined by long edges l, included angle β, short edges s, and angle γ. These

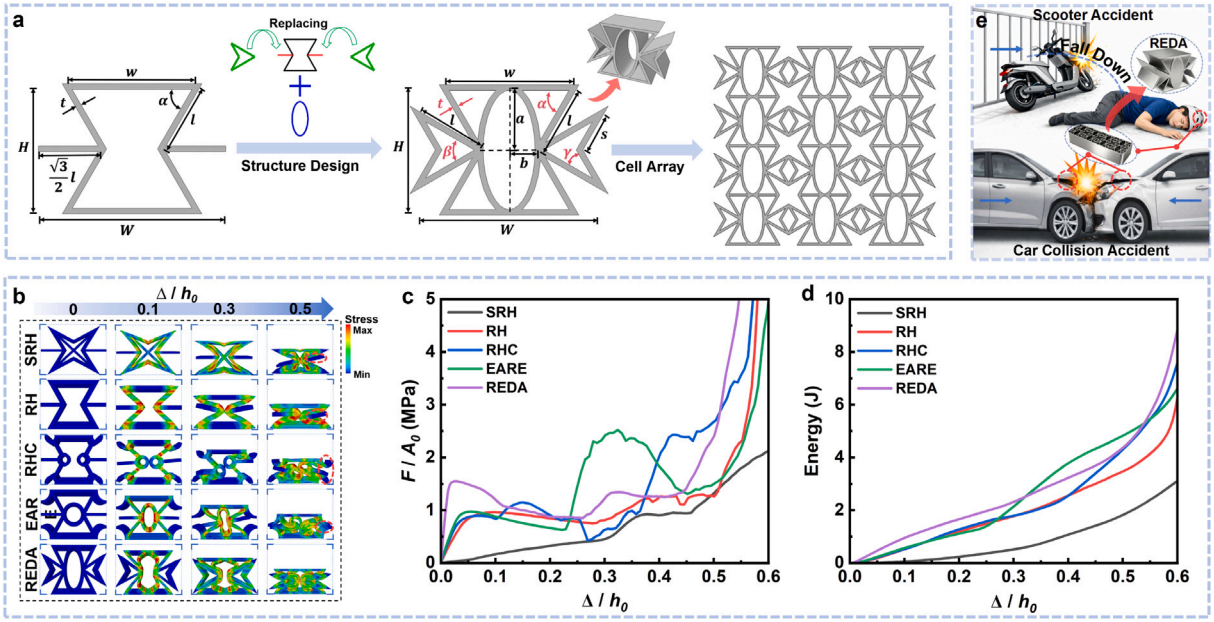

Fig. 1. Enhanced energy absorption and protective performance of the REDA hybrid structure. a. Design of the REDA structure; **b.** Numerical simulations of different unit-cell structures; **c.** Comparison of stress–strain curves among different unit-cell structures; **d.** Comparison of energy absorption (EA) performance among different unit-cell structures; **e.** Potential application of the REDA structure in vehicle collision protection.

double-arrow units introduce additional inclined load-transfer paths and provide potential plastic hinge regions during compression, thereby promoting progressive rotational deformation, improving deformation coordination, and prolonging the plastic plateau stage. Thin-walled elliptical elements with axes a and b are added between re-entrant corners and horizontal midpoints to provide internal support, redistribute local stresses, improve deformation uniformity, smooth load transfer, and suppress excessive collapse in the middle region, thereby improving stiffness, enabling multiple plastic dissipation regions, and enhancing energy absorption.

In the unit cell, all wall thicknesses are denoted by t, and the out-of-plane dimension by d, with all geometric measurements taken along the neutral axis. Based on these definitions, the corresponding parameter expressions are formulated as follows:

$$a = l \sin \alpha, \tag{1}$$

$$b = \frac{w - 2l\cos\alpha}{2}, \tag{2}$$

$$s = \frac{l \sin\left(\frac{\beta}{2}\right)}{\sin\left(\pi - \frac{\beta}{2} - \gamma\right)}, \tag{3}$$

where, a and b represent the lengths of the semi-major and semi-minor axes of the elliptical unit, and s represents the length of the short side of the double-arrow unit, respectively.

$$H = 2l \sin \alpha, \tag{4}$$

$$W = w - 2l\cos\alpha + 2l\cos\frac{\beta}{2}, \tag{5}$$

where, H and W denote the overall height and width of the unit cell, respectively.

To evaluate the energy absorption performance of the proposed structure, three key indicators were used: plateau stress (σ_p), EA, and specific energy absorption (SEA). Plateau stress represents the average stress between the initial yield strain and densification strain during compression and is calculated as the integral of stress $\sigma(\varepsilon)$ over the strain range from the initial yield strain ε_{cr} to the densification strain ε_d, divided by the total strain range, i.e., $\sigma_p = \int_{\varepsilon_{cr}}^{\varepsilon_d} \sigma(\varepsilon)\, d\varepsilon / (\varepsilon_d - \varepsilon_{cr})$, where ε_{cr} is the initial yield strain and ε_d is the densification strain. The densification strain is defined via the energy absorption efficiency η, which corresponds to the strain at the last local maximum on the efficiency-strain curve. This approach reduces subjective bias. The energy absorption efficiency is expressed as $\eta = \int_0^{\varepsilon} \sigma(\varepsilon)\, d\varepsilon / \sigma(\varepsilon)$.

EA is the total energy absorbed by the structure, equal to the area under the load–displacement curve, i.e., $EA = \int_0^{\delta_d} F(\delta)\, d\delta$, where δ_d is the densification displacement and $F(\delta)$ is the corresponding force.

SEA refers to the energy absorbed per unit mass of a structure, providing a comparison of energy absorption performance across structures with different masses. SEA is calculated as $SEA = EA/m$, where m is the mass of the structure.

2.2. Experimental details

This study employed fused deposition modeling (FDM) technology to fabricate structural specimens using polylactic acid (PLA) filament as the printing material. The specimens were produced on a Snapmaker 3D printer with a build volume of 300 × 200 ×200 mm, which accommodated the dimensional requirements of the samples. During printing, the nozzle and platform temperatures were set to 210 °C and 60 °C, respectively, with a printing speed of 50 mm/s to ensure both print quality and manufacturing efficiency.

The structural models were imported in STL format into Snapmaker Luban software for slicing and G-code generation. The build direction was set along the z-axis to minimize interference from support structures. The 3D-printed specimens featured 100% infill density, a layer height of 0.16 mm, and a wall thickness of 0.8 mm. Unless otherwise specified, all specimens were fabricated according to the geometric design shown in Fig. 1a, with the REDA unit cell defined by $l = 10$ mm, $w = 18$ mm, $t = 0.8$ mm, $d = 15$ mm, $\alpha = 60°$, $\beta = 60°$, and $\gamma = 30°$. For clarity, the detailed geometric parameters and overall dimensions of the designed specimen are further summarized in Table 1, which provides a more complete description of the structural configuration and facilitates the reproducibility of the study. To ensure the repeatability and reliability of the experimental results, three independently fabricated specimens with identical geometric parameters were prepared for each structural configuration, and each specimen was subjected to a single quasi-static compression test.

Table 1
Dimensions of the proposed REDA.

Design	Unit cells						Cellular structure		
	α (°)	β (°)	γ (°)	t (mm)	l (mm)	w (mm)	X (mm)	Y (mm)	Z (mm)
REDA	60	60	30	0.8	10	18	78.1	70.1	15

To obtain the true mechanical properties of the base material, three PLA tensile specimens were fabricated using FDM and subjected to uniaxial tensile tests in accordance with ASTM standards. The tensile tests were conducted on a universal testing machine at a loading rate of 6 mm/min. Considering the influence of the build direction on material properties during additive manufacturing, all specimens were produced using the same build direction and printing parameters as the structural samples. To ensure stable fabrication quality and geometric consistency, key printing parameters such as layer thickness, printing speed, nozzle temperature, and infill conditions were kept consistent throughout the manufacturing process. Since thin-walled regions and connection zones are more prone to geometric deviations during additive manufacturing, and such imperfections may affect local deformation, stress concentration, and the overall structural response, particular attention was paid to maintaining the geometric integrity of these critical regions during specimen preparation. Although quantitative dimensional measurements were not separately conducted, previous work by Alomarah et al. [50] has shown that manufacturing processes may affect geometric accuracy in thin-walled structures, underscoring the importance of consistent printing parameters.

In addition, the printing path and deposition strategy also play an important role in determining the dimensional consistency and anisotropic behavior of FDM-fabricated structures. Supplementary Materials Figure S1 shows the printing path and contour deposition strategy of the proposed REDA structure during FDM fabrication. It can be observed that the thin-walled cell walls are mainly formed by contour deposition rather than complex internal infill patterns such as zigzag or grid filling. Since the proposed REDA structure is a thin-walled honeycomb structure with a wall thickness of 0.8 mm and was fabricated using a 0.4 mm nozzle, the influence of infill-path-induced anisotropy is reduced. In addition, the build direction was aligned along the z-axis, while quasi-static compression loading was applied along the y-axis. Therefore, the loading direction mainly lies within the layer plane rather than along the interlayer stacking direction, which further reduces the influence of material anisotropy on the overall structural performance, and interlayer debonding is therefore not expected to dominate the collapse process. Under this configuration, the use of an equivalent isotropic constitutive model in the finite element simulation is considered reasonable for predicting the overall deformation and energy absorption response of the structure. This ensures that the deformation behavior and energy absorption response are primarily governed by the geometric configuration and thin-walled collapse behavior of the structure rather than by printing-induced anisotropy.

The tensile specimen geometry, representative fracture locations, and the corresponding stress–strain curves of three PLA specimens are shown in Supplementary Materials Figure S2. During the tensile tests, all PLA specimens fractured within the middle gauge section rather than near the clamping ends, indicating uniform stress distribution and stable loading conditions. The fracture surfaces showed typical brittle failure characteristics with limited necking deformation, which is consistent with the mechanical behavior of FDM-fabricated PLA materials under quasi-static tensile loading. The engineering stress–strain curves were obtained from the recorded load–displacement data during the tensile tests, where the stress and strain are defined as $\sigma = F/A_0$ and $\varepsilon = \Delta/H_0$, respectively. Here, F represents the applied force, A_0 is the initial cross-sectional area of the gauge section, H_0 denotes the original gauge length of the specimen, and Δ is the displacement. Based on the engineering stress–strain data, the corresponding true stress–strain relationship was further derived and used for constitutive model calibration. The yield strength of the 3D-printed PLA material was determined using the 0.2% offset method, as indicated by the dashed line in Supplementary Materials Figure S2.

Owing to the nonlinear hardening behavior of the material in the plastic region, a simplified Johnson–Cook constitutive model was developed based on the experimental data and subsequently applied in finite element simulations [51]. The present study mainly focuses on quasi-static compression behavior under relatively low loading-rate conditions, where the mechanical response is dominated primarily by progressive structural collapse and quasi-static plastic deformation. Under such conditions, the strain-rate sensitivity of PLA is relatively limited compared with medium- and high-strain-rate impact scenarios. Therefore, the strain-rate-dependent term in the Johnson–Cook constitutive model was not included in the present study. In addition, all comparative structures were analyzed using identical material properties, printing conditions, boundary conditions, and loading conditions, such that the omission of the strain-rate term is not expected to significantly influence the relative comparison of structural performance. Although incorporating strain-rate-dependent constitutive behavior would provide a more comprehensive material description for dynamic loading conditions, the simplified constitutive model adopted here is considered a reasonable approximation for quasi-static analysis and comparative structural evaluation. The corresponding tensile properties are summarized in Supplementary Materials Table S1.

2.3. Finite element model

In this study, numerical simulations of the mechanical response of the proposed structure under quasi-static compression were performed using the Abaqus/Explicit finite element platform. The material properties were obtained from the experimental results described in Section 2.2. The model was configured as a 3 × 4 unit array. As shown in Supplementary Materials Figure S3, both the loading and base plates were modeled as rigid bodies and controlled through reference points RP-1 and RP-2, respectively. The base plate was fully fixed, while the top plate was allowed to move only in the y-direction, with all other degrees of freedom constrained, thereby replicating the boundary conditions used in the experiments.

Due to the conditional stability of the explicit time integration method, the computational time step must be extremely small. Directly applying the experimental loading rate (6 mm/min) would therefore lead to excessive computational costs [52]. To evaluate the influence of loading velocity on the accuracy of the quasi-static simulations, a series of comparative analyses were conducted at compression velocities of 0.1 m/s, 0.2 m/s, 0.5 m/s, 1 m/s, and 2 m/s. Supplementary Materials Figure S4a presents the stress–strain curves obtained under different loading velocities. The results indicate that when the loading velocity did not exceed 1 m/s, the overall stress–strain responses were nearly identical, with negligible differences in plateau stress, densification behavior, and energy absorption characteristics, suggesting that the mechanical behavior of the structure was insensitive to velocity within this range [53]. However, when the loading velocity reached 2 m/s, noticeable deviations in the stress–strain response appeared, including fluctuations in plateau stress and changes in deformation stability, primarily due to the onset of inertial effects. This velocity-insensitive behavior below 1 m/s is also consistent with the quasi-static simulation strategies commonly adopted in previous studies on honeycomb and auxetic structures.

To further quantify this effect, the ratio of kinetic energy to internal energy during the compression process was monitored, as shown in

Supplementary Materials Figure S4b. At a loading velocity of 1 m/s, the kinetic energy remained below 5% of the internal energy throughout the simulation, indicating that inertial effects were negligible and that the deformation process could reasonably be regarded as quasi-static [54]. Therefore, 1 m/s was selected as the optimal loading velocity for subsequent simulations, ensuring a balance between computational efficiency and accuracy.

Subsequently, an explicit integration solver was employed to capture the nonlinear behavior arising from large deformations and multiple contact regions. To improve computational efficiency, a mass scaling strategy was applied. Contact interactions between the structure and the loading plates were modeled using the General Contact algorithm in Abaqus. This algorithm was specifically chosen due to the complex nature of the contact behavior in the structure during compression. The General Contact algorithm automatically detects all potential contact interactions, including both local contact between cell walls and self-contact between different parts of the structure. This is crucial as the REDA structure undergoes large deformations and experiences significant changes in contact regions as the deformation progresses. Furthermore, the algorithm ensures robust handling of continuously evolving contact interfaces without the need for manually defining specific contact pairs, which is essential in simulations involving progressive buckling, collapse localization, coordinated deformation, and the formation of plastic hinges. The ability to manage both local and self-contact interactions is critical for maintaining accuracy and computational stability throughout the simulation.

The effect of varying the friction coefficient from 0.1 to 0.2 on the load–displacement response was examined and found to be negligible. In this study, the friction coefficient primarily influences the tangential forces between contacting surfaces, especially in the later stages of compression. However, because the deformation behavior is dominated mainly by the bending, rotation, and progressive collapse of the thin-walled cell walls, tangential sliding between contact interfaces plays a comparatively secondary role. Consequently, the influence of friction on the global stress–strain response, particularly during the elastic and plateau deformation stages, remains minimal. The overall plateau stress and energy absorption behavior are therefore governed primarily by the structural geometry and deformation mode rather than by frictional dissipation effects. Therefore, following the recommendations in [55–57], the friction coefficient was set to 0.2, which is a typical value used in similar studies and ensures accurate results without unnecessary computational complexity.

The model was discretized using a hex-dominated mesh, with all structural elements (except the rigid loading plates) defined as C3D8R elements. A mesh convergence study was performed using four global mesh sizes, and the corresponding stress–strain responses are shown in Supplementary Materials Figure S5. The results indicate that the stress–strain responses obtained with mesh sizes of 0.5 mm and 0.4 mm are already very close, particularly in the plateau region, suggesting that the solution is approaching convergence. Further refinement to 0.3 mm leads to slight but systematic changes, while the 0.2 mm mesh introduces increased fluctuations, mainly due to enhanced numerical sensitivity associated with evolving contact interactions and local instability effects under explicit time integration. These fluctuations do not correspond to a meaningful improvement in accuracy but are more likely a consequence of numerical instability at very fine mesh resolutions. Therefore, considering both numerical stability and computational efficiency, a mesh size of 0.4 mm was selected for subsequent simulations, as it provides a stable and sufficiently converged solution without introducing excessive numerical oscillations.

2.4. Deformation mechanism and theoretical modeling of plateau stress

To establish a quantitative relationship between the structural geometry and the plateau stress, it is essential to first clarify the collapse mechanism of the unit cell under quasi-static compression. The deformation behavior governs the energy dissipation mode and ultimately determines the load-carrying capacity during the plateau stage.

In this study, preliminary finite element simulations are first conducted at the unit-cell level to investigate the deformation evolution, stress distribution, and collapse characteristics of the REDA structure under quasi-static compression. Based on the observed deformation features, including curvature localization, plastic hinge formation, and progressive rotational collapse, the theoretical model is subsequently established to capture the dominant plateau-stage deformation mechanism. As shown in Fig. 2a, a clear transition of collapse mechanism occurs with increasing strain.

When $\varepsilon < 0.02$, the inclined cell walls primarily undergo elastic bending, accompanied by slight inward deflection of the elliptical core. The deformation is distributed along the member length, and no distinct rotational centers are observed. This stage corresponds to the linear elastic regime in Fig. 2b, where the structural stiffness is governed by the bending rigidity of the cell walls. For $\varepsilon = 0.1$ and 0.20, deformation progressively localizes at the junctions between the inclined members and the central curved segment. Distinct curvature concentration zones emerge, indicating the initiation of plastic hinge formation. The inclined walls begin to rotate relative to the core, establishing identifiable rotational centers. This transition from distributed bending to localized rotation reduces the effective tangent stiffness, marking the onset of the plateau stage in Fig. 2b. These deformation characteristics provide the basis for the hinge-based analytical idealization adopted in the subsequent theoretical model. Within the strain interval $\varepsilon = 0.3$ and 0.4, a stable collapse mechanism is established. Multiple plastic hinges form and rotate coordinately, and deformation is dominated by bending-induced rotation rather than axial shortening. A collapse band gradually develops across the cell height while the members retain their structural integrity. This hinge-controlled rotational mechanism sustains an approximately constant load-carrying capacity, giving rise to the stable stress plateau observed in Fig. 2b. When $\varepsilon = 0.5$, geometric locking and intensified contact between adjacent members occur. The deformation mode transitions from hinge-controlled rotation to material compaction, leading to a rapid increase in stiffness. This corresponds to the densification regime in Fig. 2b.

To further elucidate the mechanical response from an energy perspective, the evolution of different energy components during compression is examined. As shown in Fig. 2c, the evolution of energy components indicates that the external work closely coincides with the internal energy throughout the loading process, while the kinetic energy remains negligible compared to the internal energy. Moreover, plastic dissipation dominates the internal energy during the plateau stage. These observations confirm that inertial effects are insignificant and that the external work is primarily dissipated through plastic hinge rotations. Therefore, under quasi-static conditions, the external work can be reasonably approximated as the plastic dissipation energy. To derive the plateau stress under quasi-static compression, the analytical approach of Zhang et al. [58] is adopted, assuming constant hinge lengths and deformation dominated by plastic rotation rather than axial member strain. Based on the unit-cell deformation in Figs. 2d–2f, a theoretical model using energy conservation, which equates external work to hinge energy dissipation, yields the analytical plateau stress.

Under continuous compression, the re-entrant honeycomb cells contract inward, engaging the internal elliptical and double-arrow cells to form a stable, uniform deformation mode, Fig. 2e illustrates this process. In this figure, the red circles indicate regions of curvature concentration where significant plastic bending is expected during the plateau stage, which are assumed to act as the locations of plastic hinges and corresponding rotation centers in the analytical model. These regions correspond closely to the stress concentration zones highlighted in red in Fig. 2a. The stress concentration is mainly distributed near the junctions between the re-entrant walls and double-arrow

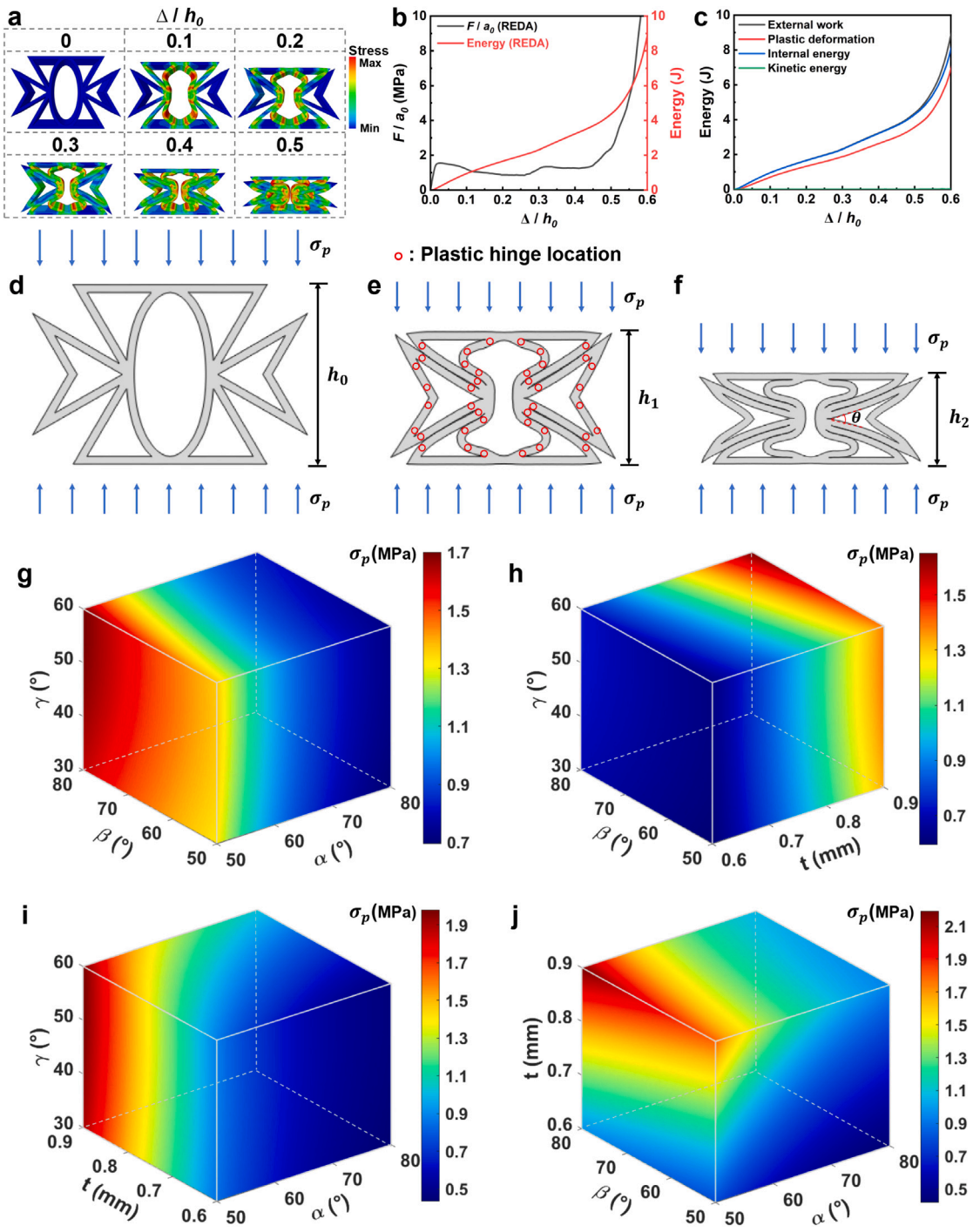

Fig. 2. Deformation evolution and energy dissipation mechanisms of the REDA structure. a. Progressive deformation modes of the REDA unit cell under quasi-static compression; **b.** Stress–strain response and corresponding energy absorption evolution; **c.** Evolution of energy components during quasi-static compression; **d.** Initial configuration; **e.** Intermediate configuration; **f.** Densified configuration; **g.** Effect of parameters α, β, and γ on plateau stress; **h.** Effect of parameters t, β, and γ on plateau stress; **i.** Effect of parameters α, t, and γ on plateau stress; **j.** Effect of parameters α, β, and t on plateau stress.

units, the arrow-tip regions, and the connections between the elliptical segments and adjacent inclined members. Therefore, the assumed rotation centers are established based on deformation compatibility and stress localization observed in the finite element simulations. The consistency between the stress localization observed in Fig. 2a and the curvature concentration assumed in Fig. 2e supports the formation of plastic hinges at these locations and validates the hinge-based analytical model.

For the analytical model, the compression process is considered up to a characteristic deformation state in which the included angle of the double-arrow unit is taken as one half of β. Based on the geometric relationships of the unit cell, the rotation angles of the structural members can then be determined. Due to the continuously varying curvature of the elliptical segment, it is difficult to directly define a unique rotation angle as in straight members. Therefore, an equivalent geometric approximation is adopted. Specifically, the rotation angle of the elliptical segment is evaluated at a representative location corresponding to half of the major axis ($\frac{a}{2}$), where the most representative deformation behavior occurs, and is approximated as the average of two deformation components associated with compression towards the

Table 2
Comparison of plateau stress predictions with and without correction factor k.

α (°)	FEA (MPa)	Without k		With k	
		Theory (MPa)	Error (%)	Theory (MPa)	Error (%)
50	1.602	1.349	15.79	1.504	6.12
60	1.121	1.110	0.98	1.109	1.07
70	0.916	0.983	6.81	0.891	2.73
80	0.737	0.922	20.07	0.771	4.41

horizontal boundary and along the inclined edge. This treatment is consistent with the deformation morphology observed in the finite element simulations, where the regions of curvature concentration correspond well to the locations of maximum stress. This approximation allows the dominant deformation tendency of the elliptical segment to be incorporated into the hinge-based analytical framework while maintaining analytical tractability. Specifically, the rotation angles of the long edges and short edges of the double-arrow cells, the re-entrant honeycomb members, and the elliptical segments can be represented by θ_1, θ_2, θ_3, and θ_4, respectively, which are expressed as follows:

$$\theta_1 = \beta - \theta, \tag{6}$$

$$\theta_2 = \gamma - \frac{\theta}{2}, \tag{7}$$

$$\theta_3 = \alpha - \frac{\theta}{2}, \tag{8}$$

$$\theta_4 = \frac{1}{2}\arctan\frac{2\sqrt{3}l\sin\alpha}{3(w-2l\cos\alpha)} + \frac{1}{2}\arctan\frac{(2-\sqrt{3})(w-2l\cos\alpha)}{2l\sin\alpha} + \frac{\pi-\theta}{4}. \tag{9}$$

In the theoretical derivation, a rigid-plastic hinge model is adopted to describe the plastic energy dissipation of structural units. For straight struts, these locations are idealized as discrete plastic hinges. However, for the elliptical curved segments, the plastic dissipation is evaluated through continuous path integration of bending energy rather than assuming localized hinge formation. According to Mo et al. [42], horizontal beams are treated as secondary structural members with limited direct contribution to vertical load resistance under the bending-dominated deformation mode considered in this study. In the present configuration, bending in the inclined edges and elliptical segments governs the overall structural response during the plateau stage. While the horizontal beams help reduce stress concentration and improve deformation coordination between adjacent unit cells, their role in vertical crushing resistance is not dominant within the plateau deformation regime. The re-entrant honeycomb cells form 8 plastic hinges. The double-arrow cells contribute an additional 16 hinges, with eight located along the long edges and the remaining eight along the short edges. The contribution of the elliptical segments is obtained through path-integrated bending energy, consistent with their continuously varying curvature and distributed deformation characteristics observed in both simulations and experiments. This treatment is particularly appropriate for the plateau-stage response under quasi-static compression, where bending-induced progressive collapse is the dominant energy dissipation mechanism.

However, structural units contribute unequally to deformation, and the elliptical segment cannot be fully represented by an idealized discrete hinge. Due to its continuously varying curvature, the bending moment and axial force distribution along the ellipse is non-uniform, which may lead to an overestimation of energy dissipation under certain geometric configurations. This discrepancy is particularly sensitive to the re-entrant angle α, since the effective perimeter and deformation path of the ellipse vary significantly with α. The sensitivity to α arises from the variation in geometric coupling between the elliptical reinforcement and surrounding inclined members, which alters the local curvature distribution and deformation path. To equivalently account for this curvature-induced effect, a geometry-dependent correction factor $k(\alpha)$ is introduced and applied specifically to the plastic hinge contribution of the elliptical unit, taking the inclined edge of the re-entrant cell as the reference deformation path. The factor $k(\alpha)$ further reflects the influence of geometric nonlinearity and non-uniform bending in the curved segments, and is calibrated based on the plateau stress obtained from finite element simulations, thereby incorporating the geometry-dependent deformation characteristics that are not captured by the idealized hinge model. The total energy dissipated by plastic hinge rotation is thus modified accordingly. To quantitatively evaluate the effectiveness of this correction, a comparative analysis of plateau stress predictions with and without $k(\alpha)$ is presented in Table 2. It can be observed that incorporating $k(\alpha)$ significantly reduces the prediction error across different values of α, thereby improving the predictive consistency of the theoretical model without altering its fundamental deformation mechanism. Based on the above deformation mechanism and the modified hinge contributions, the total plastic energy dissipation can be expressed as:

$$E_p = 8\theta_1 M_{p1} + 8\frac{l}{s}\theta_2 M_{p2} + 8\theta_3 M_{p3} + \frac{4l}{L_{\text{ellipse}}} k I_{\text{ellipse}} \theta_4 M_{p4}, \tag{10}$$

where L_{ellipse} denotes the approximate ellipse perimeter, and I_{ellipse} is the total effective rotation obtained from the boundary integral, characterizing the ellipse's energy dissipation. The weighting factors $\frac{l}{s}$ and $\frac{4l}{L_{\text{ellipse}}}$ correspond to the short-side deformation of the double-arrow unit and the elliptical unit, respectively. The perimeter of the ellipse is approximated using a standard analytical expression as:

$$L_{\text{ellipse}} = \pi\left[3(a+b) - \sqrt{(3a+b)(a+3b)}\right], \tag{11}$$

exploiting the geometric symmetry of the ellipse, the boundary integration of the bending contribution is evaluated over one quarter of the curve and multiplied by four, and can be expressed as:

$$I_{\text{ellipse}} = 4\int_0^{\frac{\pi}{2}} \frac{ab}{a^2\sin^2\theta + b^2\cos^2\theta}\, d\theta. \tag{12}$$

While $k(\alpha)$ is a correction factor dependent on α, applied to correct the bending contribution of the elliptical segments, and is expressed as:

$$k = 0.3705\alpha^2 - 1.5526\alpha + 2.218, \tag{13}$$

where α is converted from degrees to radians. The plastic moments M_{p1}, M_{p2}, M_{p3}, and M_{p4} denote the plastic bending moments of the long edges of the double-arrow unit, the short edges of the double-arrow unit, the re-entrant honeycomb members, and the elliptical segments, respectively, and can be expressed as:

$$M_{p1} = M_{p2} = M_{p3} = M_{p4} = \frac{\sigma_o d t^2}{4}, \tag{14}$$

where d is the out-of-plane thickness of the structure and σ_o is the yield stress of an ideal elastic–plastic material. To account for deviations from ideal elastic–plastic behavior in real materials, a yield-stress correction is introduced. In strain-hardening materials, the stress governing plastic collapse is not strictly equal to the initial yield stress but reflects an averaged response over the plastic strain range. Accordingly, an equivalent flow stress, denoted as σ_o, is adopted to approximate the average bending resistance during plastic hinge rotation. This formulation is suitable for materials with moderate strain hardening, such as the PLA used in this study. For materials that deviate from ideal elastic-perfectly plastic behavior, the equivalent flow stress should be defined according to an appropriate constitutive representation. Following the

treatment proposed by Zhu et al. [59] and Wen et al. [60], a simplified engineering approximation is adopted to account for the non-ideal plastic response in quasi-static collapse analysis. In this study, consistent with rigid-plastic hinge-based formulations, the equivalent flow stress is approximated as the average of the yield stress and ultimate tensile strength, representing an effective plastic resistance over the strain-hardening range. This provides a reasonable estimation of the stress level governing plastic hinge rotation under quasi-static conditions. Accordingly, the equivalent flow stress is expressed as:

$$\sigma_o = \frac{\sigma_s + \sigma_u}{2}, \tag{15}$$

where σ_s and σ_u are the yield stress and ultimate tensile strength, respectively.

Additionally, the external work acting on the unit cell is expressed as:

$$W_p = \sigma_p L_0 d \Delta_L, \tag{16}$$

where σ_p denotes the quasi-static plateau stress, L_0 the initial unit-cell length, and Δ_L the deformation length. The corresponding expression is derived from the deformation mode and geometric relations as follows:

$$L_0 = w, \tag{17}$$

$$h_0 = H, \tag{18}$$

$$\Delta_L = h_0 - h_2 = 2l(\sin\alpha - \sin\tfrac{\beta}{4}). \tag{19}$$

Finally, based on the energy conservation equation $E_p = W_p$, the theoretical expression of the plateau stress of the structure can be derived as:

$$\sigma_p = \frac{E_p}{L_0 d \Delta_L} = \frac{\sigma_0 t^2 \left(2\left(\alpha + \frac{\beta}{4} + \frac{l}{s}\gamma\right) + \frac{l}{L_{\text{ellipse}}} k I_{\text{ellipse}} \theta_4\right)}{2lw\left(\sin\alpha - \sin\frac{\beta}{4}\right)}. \tag{20}$$

where θ_4, L_{ellipse}, I_{ellipse}, and k are given by Eqs. (9), (11), (12) and (13).

The above formulation is derived under several simplifying assumptions, including the rigid–plastic hinge idealization, the neglect of axial deformation in the structural members, the use of an equivalent flow stress to represent material yielding behavior, and the geometric simplification adopted for the rotation and deformation of the elliptical segment. These assumptions are primarily intended to simplify the analytical treatment while retaining the dominant bending-controlled collapse mechanism observed in the proposed structure during quasi-static compression. The proposed theoretical model is most applicable to deformation conditions dominated by localized bending and plastic hinge formation, particularly for relatively slender thin-walled honeycomb structures subjected to quasi-static in-plane compression. Under such conditions, the energy dissipation process is mainly governed by progressive plastic rotation concentrated in localized regions of the unit cell, which is consistent with the deformation patterns observed in both the finite element simulations and compression experiments.

However, the applicability of the analytical formulation may become limited when axial stretching or membrane deformation becomes significant, when material strain hardening and nonlinear constitutive behavior dominate the response, when severe geometric nonlinearities occur under large deformation, or when local instability and buckling modes deviate from the assumed collapse mechanism. In addition, the predictive accuracy may decrease when the deformation behavior of the elliptical segment no longer follows the simplified kinematic assumptions adopted in the derivation. Therefore, the present model should be regarded as a simplified analytical approximation intended to capture the dominant first-order deformation mechanism and the relative influence of geometric parameters on plateau stress, rather than a fully comprehensive constitutive description applicable to all loading conditions and structural scales. Detailed finite element simulations and experimental investigations remain necessary for accurately predicting the complete nonlinear response of the structure under complex loading conditions.

Under these conditions, the influence of geometric parameters on σ_p can be further examined. Figs. 2g–2j presents the variation of plateau stress for different parameter conditions based on the theoretical formulation. Since the plateau stress is jointly governed by four variables, namely the wall thickness t and the three angle parameters (α, β, γ), the theoretical relationship corresponds to a four-dimensional parameter space. For the sake of clarity and interpretability, this study adopts a controlled-variable approach, where in each analysis one parameter is held constant and only combinations of the other three parameters are discussed. This approach ensures a systematic investigation of the main factors and their synergistic effects, while also allowing the trends to be clearly illustrated in the figures. Based on these trends, the following sections will discuss the effect of each parameter as well as the mechanisms of mutual cancellation and synergy.

As shown in Fig. 2g, the plateau stress varies with α, β, and γ. Increasing α has a pronounced negative effect, leading to a significant reduction in plateau stress, whereas increasing β and γ exerts positive effects, with β being more influential than γ. The positive contributions of β and γ can partially offset the reduction caused by increasing α, particularly when α is relatively small. However, at larger α, its negative effect dominates, resulting in an overall decrease in plateau stress. Fig. 2h illustrates the combined influence of t, β, and γ, all of which positively affect the plateau stress. Among them, t plays the dominant role, followed by β and then γ. Their consistent effects lead to a clear synergistic enhancement, in which increasing t not only directly raises the plateau stress but also strengthens the contributions of β and γ. Figs. 2i and 2j show the variations in plateau stress with the parameter combinations (α, t, γ) and (α, β, t), respectively. In both cases, t and α exhibit opposing effects, with t providing a strong positive contribution and α producing the most significant negative influence. Although the effects of β and γ are weaker, they partially offset the reduction caused by increasing α, maintaining high plateau stress at larger t.

In summary, the plateau stress is dominated by the wall thickness t, which provides the strongest enhancement. Increasing α markedly reduces the plateau stress, whereas β and γ have weaker positive effects. A high plateau stress is therefore obtained with large t, small α, and relatively large β and γ, highlighting the dominant role of thickness and the secondary compensatory effect of the angle parameters.

3. Results and discussion

3.1. Experimental results and finite element (FE) model validation

This section primarily compares the experimental results of the REDA structure under quasi-static compression with those obtained from finite element analysis (FEA), followed by an analysis and discussion of its deformation modes.

Fig. 3a and 3b show that the experimental and numerical stress–strain responses and the corresponding deformation stages of the REDA structure are in good agreement. However, a slight discrepancy can be observed in the low-strain region, which may be attributed to local geometric deviations in the printed specimens, such as thin-wall regions, as well as the idealized material and geometric assumptions adopted in the finite element model. As shown in Table 3, the experimentally measured plateau stresses are 1.048 MPa, 1.071 MPa, and 1.108 MPa, while the finite element result is 1.121 MPa, corresponding to relative errors of 6.51%, 4.46%, and 1.16%, respectively. The theoretical prediction is 1.109 MPa, which differs from the experimental results by 5.50%, 3.43%, and 0.09%, respectively, and shows a deviation of 1.07% from the finite element result, indicating that the proposed analytical model can effectively capture the dominant deformation

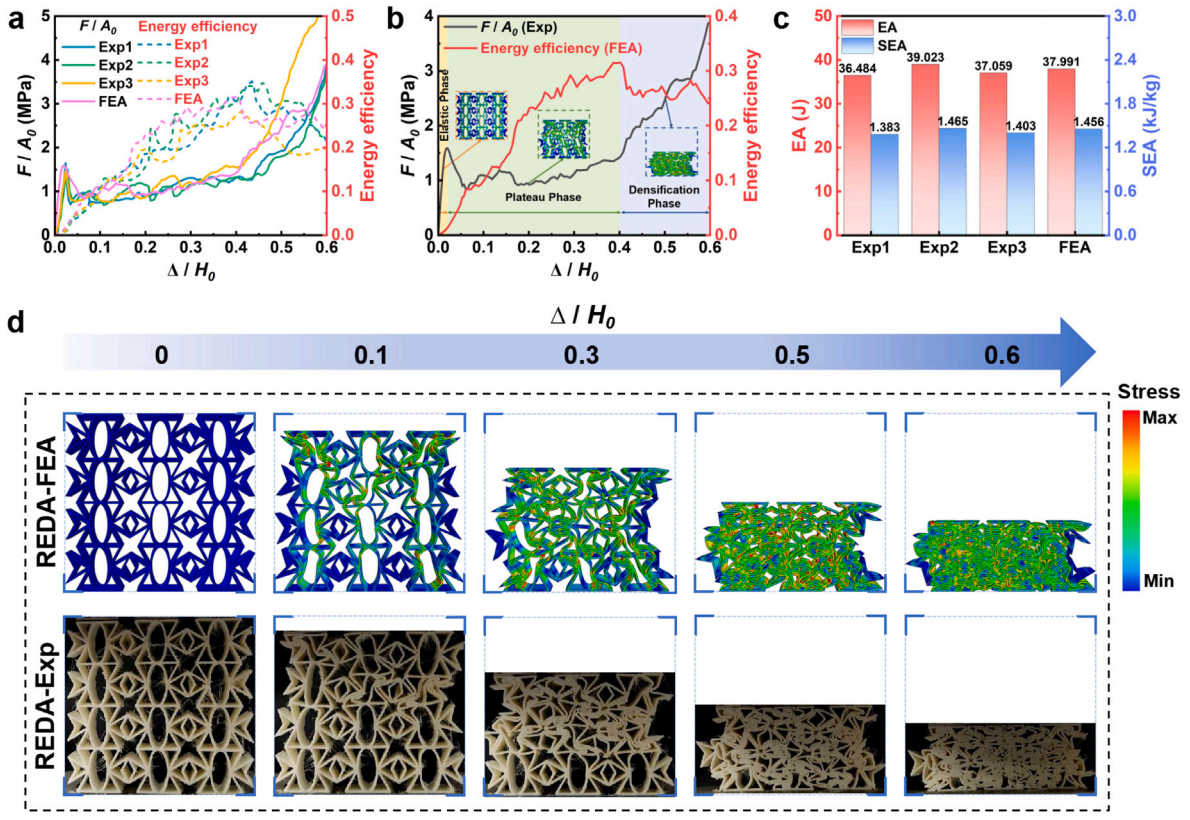

Fig. 3. Comparison between experimental results and finite element analysis. **a.** Stress–strain curves of REDA in experiment and finite element results; **b.** Schematic diagram of the three stages of REDA under quasi-static compression; **c.** Comparison of EA and SEA in experiment and finite element analysis; **d.** Deformation comparison between experiment and finite element results.

Table 3
Experimental and FEA results with errors.

Sample	Plateau stress (MPa)	EA (J)	SEA (kJ/kg)
FEA	1.121	37.991	1.456
Exp1	1.048	36.484	1.383
Error (%)	6.51	3.97	5.01
Exp2	1.071	39.023	1.465
Error (%)	4.46	2.64	0.61
Exp3	1.108	37.059	1.403
Error (%)	1.16	2.45	3.64
Exp Mean	1.075	37.522	1.417
Exp SD	0.03	1.33	0.04
Error Mean (%)	4.04	2.68	3.42

mechanism and provide accurate prediction of the plateau stress under quasi-static compression. The observed deviations can be attributed to the simplifying assumptions in the theoretical model, as well as experimental uncertainties such as manufacturing imperfections. Fig. 3c shows good agreement between the experimental and numerical EA and SEA values. The EA errors are 3.97%, 2.64%, and 2.45%, while the SEA errors are 5.01%, 0.61%, and 3.64%, respectively. The statistical results presented in Table 3 indicate that the standard deviations of plateau stress, EA, and SEA are 0.03 MPa, 1.33 J, and 0.04 kJ/kg, respectively, demonstrating relatively small variations among repeated tests and thus good experimental repeatability. Furthermore, the mean relative errors between experimental and numerical results are 4.04%, 2.68%, and 3.42%, respectively, indicating satisfactory consistency between experiments and simulations.

As shown in Fig. 3d, the experimental and numerical deformation modes exhibit overall consistent deformation patterns, while local non-uniformity can still be observed. The discrepancies between experimental and numerical results may arise from several factors. The numerical model assumes homogeneous isotropic material behavior, whereas FDM-fabricated PLA inherently exhibits anisotropy due to its layer-wise deposition process, interfacial bonding variations, and local material heterogeneity, which may slightly influence the predicted stiffness and collapse stress. In addition, manufacturing imperfections introduced during the printing process also contribute to the deviations. Notably, locally thin walls were directly observed in certain regions of the printed specimens, which are more susceptible to deformation and can trigger premature local instability under compressive loading. These regions tend to experience uneven load distribution, leading to a slight reduction in plateau stress and energy absorption capacity. Furthermore, defects such as micro-voids, insufficient interlayer bonding, and possible local damage or delamination during compression may further influence the experimental response. These effects are not explicitly included in the finite element model, which assumes idealized geometry and homogeneous material behavior. Nevertheless, the overall agreement remains satisfactory, indicating that the adopted modeling strategy provides sufficient accuracy for the present study.

As shown in Fig. 3b, the stress–strain response of the REDA structure under quasi-static compression exhibits three deformation stages: the linear elastic stage (yellow), the plastic plateau stage (green), and the densification stage (blue). Representative deformation configurations corresponding to $\varepsilon = 0.01$, 0.20, and 0.50 are illustrated in the embedded contour plots, which characterize the elastic, plateau, and densification stages, respectively.

In the linear elastic stage, the REDA structure undergoes geometry-dominated deformation, characterized by inward rotation of the re-entrant edges and slight flattening of the elliptical units, while maintaining overall elastic integrity. As the strain increases, the structure

Table 4
Geometric parameters of different honeycomb structures.

Design	α (°)	β (°)	γ (°)	φ (°)	t (mm)	l (mm)	w (mm)	a (mm)	b (mm)	s (mm)	r_1 (mm)	r_2 (mm)
RHC	60	–	–	–	1.256	10	18	–	–	–	2	–
RH	60	–	–	–	1.556	10	18	–	–	–	–	–
SRH	–	–	–	30°	0.953	10	–	–	–	–	–	–
EARE	60	–	–	–	1.011	10	18	–	–	–	–	4
REDA	60	60	30	–	0.8	10	18	$5\sqrt{3}$	4	$\frac{10}{\sqrt{3}}$	–	–

enters the plastic plateau stage, where cooperative deformation between the re-entrant and elliptical units contributes to enhanced the energy absorption capacity. The re-entrant edges primarily deform through hinge-controlled rotation, whereas the elliptical units gradually flatten, providing additional buffering resistance. This sequential deformation mechanism delays the onset of structural instability and promotes a relatively stable load-bearing response. Moreover, the deformation exhibits an overall progressive collapse pattern, while local non-uniformity and asynchronous deformation of individual cells may occur during compression. Moreover, the interaction between the two geometries redistributes the load-transfer path and increases the number of plastic hinges formed within the structure. The interfaces between the re-entrant edges and elliptical units act as additional deformation zones, enabling an overall gradual collapse with spatially distributed but locally non-uniform deformation, which results in enhanced energy dissipation compared to the independent deformation modes of each unit. As compression continues, contact between the inclined edges of the re-entrant units and the long edges of the double-arrow units induces local load-bearing and buckling, forming multiple plastic hinges that prevent sudden collapse. Finally, in the densification stage, progressive pore closure leads to plastic compaction and a sharp increase in stress.

3.2. Comparison with existing structures

This section evaluates the mechanical response and energy absorption performance of the REDA structure through two comparative cases. In the first case, REDA is compared with the conventional re-entrant honeycomb (RH) under identical wall thickness conditions. Since RH represents the fundamental parent topology from which the REDA structure is developed, this comparison is intended to directly evaluate the influence of the incorporated elliptical reinforcement units and double-arrow components on the deformation mode, load-transfer behavior, plateau stress, and energy absorption characteristics relative to the original re-entrant framework.

In the second case, REDA is compared with RH, RHC, EARE, and SRH under identical relative density conditions. These structures were selected because they represent several typical re-entrant, reinforced, and hybrid auxetic honeycomb configurations closely related to the design philosophy of the proposed REDA structure. Specifically, RHC was selected as a representative boundary-reinforced re-entrant honeycomb structure with circular reinforcements near the re-entrant joints [40]. EARE was selected as a representative curved-element reinforced re-entrant honeycomb structure containing embedded elliptical annular components [39]. In addition, SRH was included as a representative hybrid internally reinforced honeycomb structure, as it combines star-shaped and rhombic units to introduce internal constraints and additional load-transfer paths [41]. The comparison under identical relative density was adopted to reduce the influence of material usage differences, allowing the effects of structural configuration on plateau stress, deformation stability, and energy absorption performance to be evaluated more reasonably.

3.2.1. Comparison under identical wall thickness

As shown in Fig. 4a and 4b, under identical wall thickness, the REDA structure exhibits a significantly higher plateau stress than RH under quasi-static compression, with finite element results of 1.121 MPa versus 0.155 MPa, respectively, representing an increase of more than sixfold. This improvement is attributed to the additional internal support and constraint provided by the elliptical and double-arrow hybrid units. Compared with the conventional RH structure, these hybrid components enhance the structural stiffness and improve the continuity of deformation during compression, resulting in a more stable and sustained stress plateau response. Consequently, as shown in Fig. 4c, the EA and SEA of REDA reach 37.991 J and 1.456 kJ/kg, compared with 3.168 J and 0.236 kJ/kg for RH, increasing nearly elevenfold and more than fivefold, respectively. These results clearly demonstrate the superior energy absorption capability of the REDA structure under quasi-static compression.

These results demonstrate that the REDA structure, through its enhanced internal support and stable cooperative deformation mechanism, not only achieves significant improvements in plateau stress and energy absorption capacity but also exhibits more stable and controllable global deformation behavior during compression.

Fig. 4d shows that under quasi-static compression, the RH structure evolves from initially symmetric deformation to pronounced asymmetric buckling (at $\varepsilon = 0.1$). As the strain increases, instability initiates near the loading and fixed ends and propagates toward the center, leading to lateral offset and uneven collapse (at $\varepsilon = 0.3$). At higher strains, inter-unit contact and densification occur, accompanied by highly asymmetric deformation (at $\varepsilon = 0.5$ and 0.6). This behavior arises from boundary effects, limited lateral stiffness, and early local unit instability, despite the geometrically symmetric design of the RH structure.

The REDA structure demonstrates superior deformation stability and energy dissipation throughout compression. Only localized components buckle initially, with the upper region forming a V-shaped deformation ($\varepsilon = 0.1$). As compression progresses, the lower region develops an inverted V-shaped band, producing an X-shaped symmetric buckling mode ($\varepsilon = 0.3$). This cooperative mechanism persists through the plastic plateau, delaying local instability and ensuring smooth stress transfer. During densification, unit contact and compaction intensify ($\varepsilon = 0.5$), and at full densification, symmetry is maintained without significant asymmetric collapse ($\varepsilon = 0.6$). Overall, the progressive formation and coordinated evolution of the V-shaped bands prolong the plastic plateau, control collapse propagation, and enhance energy absorption, highlighting REDA's superior stability compared with RH.

3.2.2. Comparison under identical relative densities

A comparative analysis of the energy absorption of RHC, RH, SRH, EARE, and REDA was conducted at the same relative density. The schematics are shown in Fig. 5a. EARE and RHC dimensions follow Fig. 1a, with EARE's re-entrant units assumed identical to REDA and containing an embedded circle of radius b, while RHC replaces each re-entrant corner with a circle of radius $\frac{b}{2}$. In addition, the SRH structure incorporates an internal star-shaped reinforcement with a star angle of 30°. The detailed geometric parameters of the different structures are listed in Table 4. The relative density expressions for RHC, RH, SRH, EARE, and REDA are as follows:

$$\rho_{RHC} = \frac{(2(w-b)+4(l-b)+\sqrt{3}l-b+4\pi b)t}{2l\sin\alpha\times(\sqrt{3}l+w-2l\cos\alpha)}, \tag{21}$$

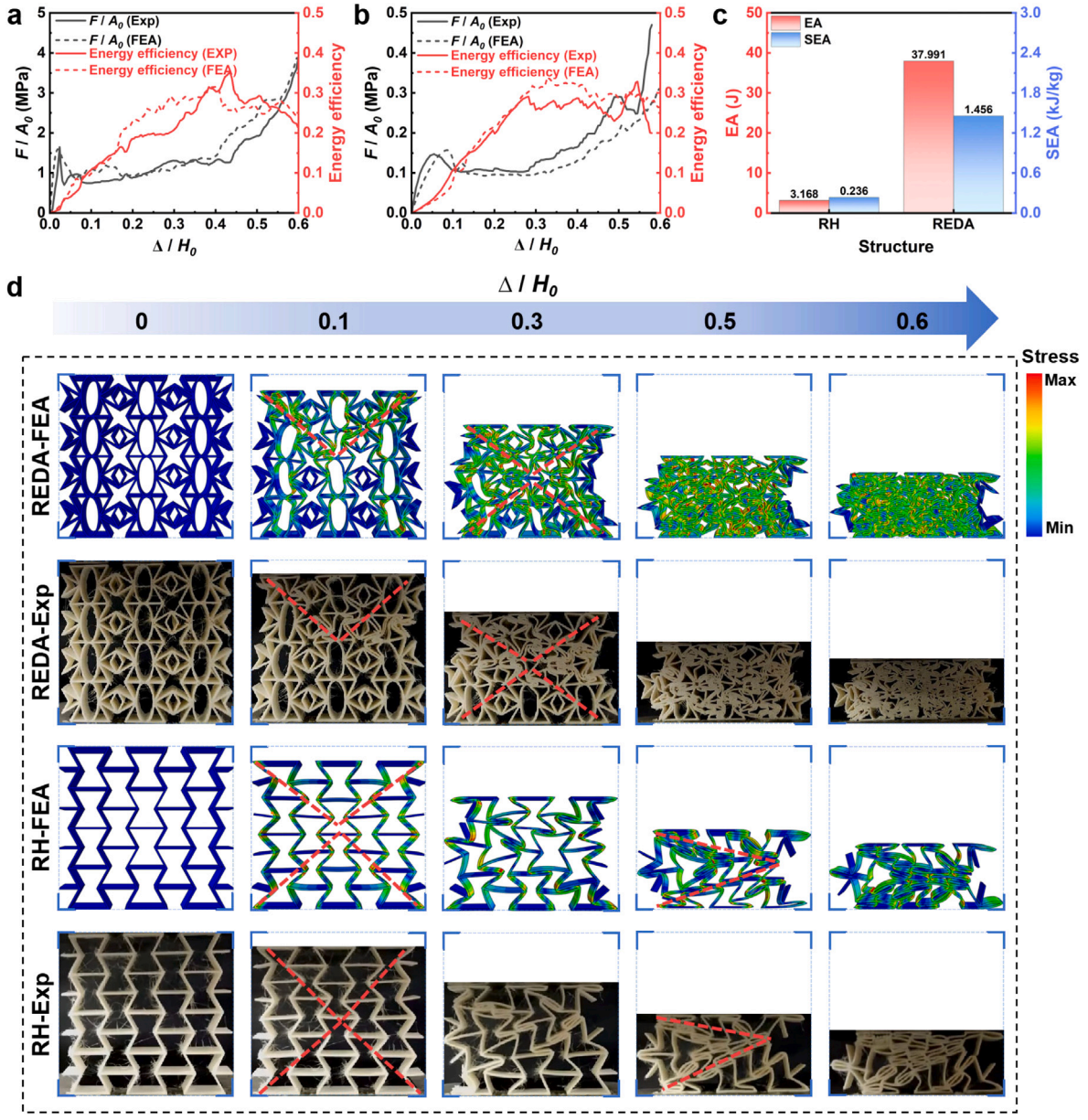

Fig. 4. Comparison of structures under identical unit cell dimensions. a. Comparison between experimental and finite element stress–strain curves of REDA; **b.** Comparison between experimental and finite element stress–strain curves of RH; **c.** Comparison of finite element EA and SEA for the two structures; **d.** Comparison of experimental and finite element results of REDA and RH under quasi-static compression.

$$\rho_{RH} = \frac{(2w + (4+\sqrt{3})l)t}{2l\sin\alpha \times (\sqrt{3}l + w - 2l\cos\alpha)}, \tag{22}$$

$$\rho_{SRH} = \frac{\left((8+\sqrt{3})l + 4\sqrt{2}l\cos\varphi\right)t}{2l\cos\varphi \times \left(\sqrt{3}l - 2l\sin\varphi + 2l\cos\varphi\right)}, \tag{23}$$

$$\rho_{EARE} = \frac{(2w + (4+\sqrt{3})l + 4\pi b)t}{2l\sin\alpha \times (\sqrt{3}l + w - 2l\cos\alpha)}, \tag{24}$$

$$\rho_{REDA} = \frac{(8l + 2w + 4s + 2\pi\sqrt{\frac{a^2+b^2}{2}})t}{2l\sin\alpha \times (\sqrt{3}l + w - 2l\cos\alpha)}. \tag{25}$$

As shown in Fig. 5b, the hybrid re-entrant honeycomb structures exhibit distinct stress–strain behaviors due to differences in their internal reinforcement mechanisms and load-transfer paths. The RH structure primarily relies on the bending deformation of inclined cell walls and shows an initial stress peak followed by a relatively low and unstable plateau stress. This behavior indicates insufficient internal support during progressive compression, resulting in limited sustained load-bearing capacity and relatively low energy absorption. The RHC structure enhances the re-entrant corners through circular reinforcements, which increases local stiffness during the intermediate deformation stage. As compression proceeds, repeated contact and separation between neighboring circular regions cause multiple sharp stress rises and drops, resulting in pronounced stress oscillations and discontinuous deformation behavior. Although the local reinforcement delays collapse in some regions, the load transfer across the entire structure remains non-uniform.

The SRH structure introduces star-shaped internal reinforcements, which improve the continuity of load transfer during compression. The additional internal members participate in deformation and provide a smoother stress response together with a slightly enhanced plateau stress. However, because the reinforcement effect is mainly concentrated near the central region of the unit cell, the overall improvement

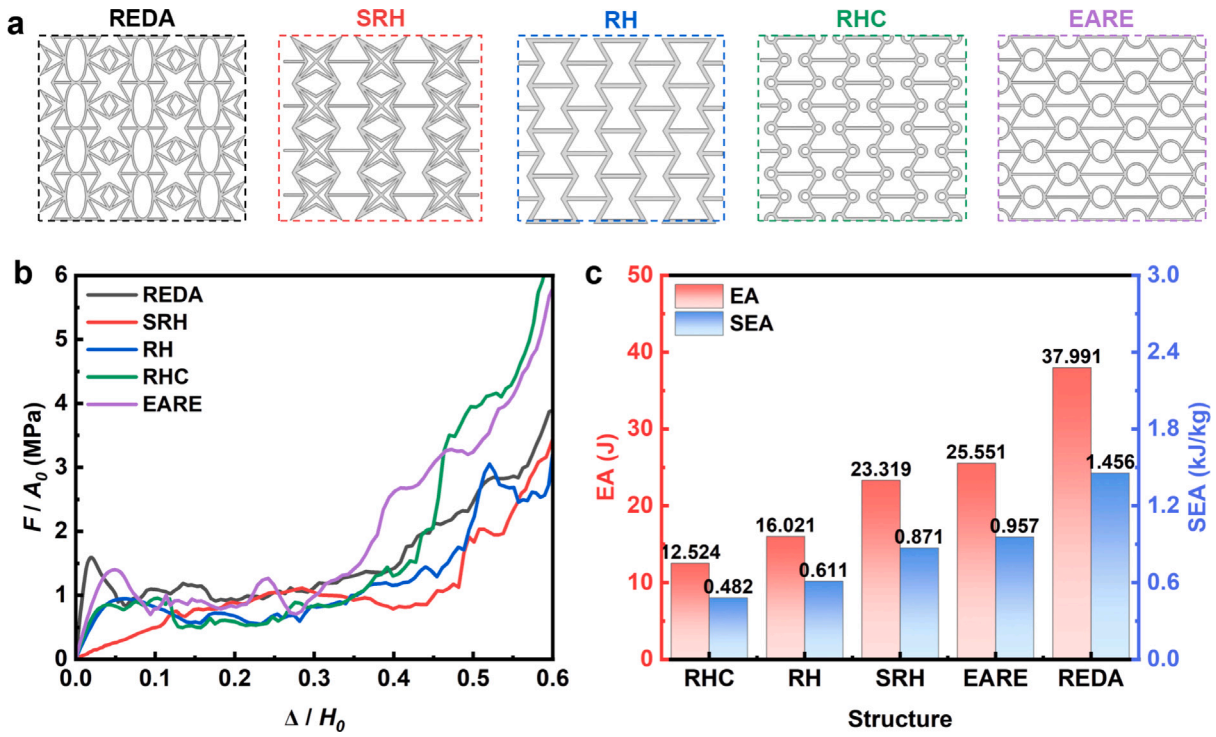

Fig. 5. Comparison of structures under the same relative density. a. Schematic diagrams of REDA, SRH, RH, RHC and EARE structures; **b.** Comparison of stress–strain curves for these five structures; **c.** Comparison of EA and SEA for these five structures.

in energy absorption remains limited, and the stress level is still lower than that of the reinforced hybrid configurations. The EARE structure exhibits a relatively high stress level during the early stage of compression because the embedded elliptical annular components provide additional resistance against inward bending deformation. However, the stress plateau is relatively short, and the structure enters the densification stage at a comparatively small strain. As a result, the effective plastic deformation range is limited, reducing the contribution of the medium-strain region to the overall energy absorption performance.

In contrast, the REDA structure combines elliptical reinforcement with double-arrow load-transfer units, enabling more coordinated deformation throughout the compression process. The elliptical components provide continuous internal support, while the double-arrow connections promote stress redistribution between adjacent cells. Consequently, the REDA structure maintains a relatively stable and prolonged plateau stress within the strain range of approximately $\varepsilon = 0.1$ to 0.4, effectively delaying densification and suppressing severe stress fluctuations. The extended plastic deformation stage results in a larger area under the stress–strain curve, thereby providing significantly enhanced energy absorption capacity prior to densification.

The Poisson's ratio of each structure was calculated as the negative ratio of the transverse strain to the axial strain under quasi-static compression, i.e., $\nu = -\varepsilon_x/\varepsilon_y$, where ε_x and ε_y are the transverse and axial strains, respectively. This auxetic behavior mainly originates from the rotational deformation of the inclined re-entrant cell walls under compression, while the internal reinforcement units further influence the deformation coordination and transverse constraint within the unit cell. Following the methodology proposed by Esmaeili et al. [61], an axial strain level of 0.02 was selected for the calculation of the negative Poisson's ratio in order to characterize the initial auxetic deformation behavior within the small-strain regime.

For the conventional RH and RHC structures, the inclined cell walls are relatively free to rotate during compression, producing strong lateral contraction with negative Poisson's ratios of approximately −1.014 and −1.263, respectively. Although this relatively large rotational freedom enhances the magnitude of the auxetic response, it may also promote excessive transverse deformation, stress concentration, and non-uniform collapse during progressive compression. By contrast, the EARE structure, which incorporates elliptical internal reinforcement, exhibits a smaller magnitude of negative Poisson's ratio of approximately −0.813. The elliptical units partially constrain excessive transverse contraction and regulate the rotational deformation of the inclined members while still preserving auxetic behavior, thereby improving deformation coordination and compression stability.

The proposed REDA structure, which combines elliptical reinforcement with double-arrow load-transfer components, exhibits a negative Poisson's ratio similar to that of EARE, approximately −0.813. The elliptical units provide continuous internal support and suppress excessive inward collapse, while the double-arrow members facilitate progressive rotational deformation and stress redistribution between adjacent cells. As a result, the REDA structure maintains coordinated auxetic deformation over a broader strain range and simultaneously exhibits improved plateau stress stability, delayed densification, and enhanced energy absorption performance.

In addition, the SRH structure, incorporating strong star-shaped internal reinforcements, exhibits the smallest magnitude of negative Poisson's ratio, approximately −0.281. The strong geometric constraint imposed by the star-shaped members suppresses transverse contraction and limits the rotational deformation of the inclined walls, thereby reducing the auxetic effect.

These observations indicate that a larger magnitude of negative Poisson's ratio does not necessarily correspond to superior mechanical performance. Excessive lateral contraction may reduce deformation stability and accelerate instability propagation during compression. By contrast, moderate restriction of transverse deformation through internal reinforcement can improve deformation coordination, delay local buckling, stabilize the plateau stress response, and enhance energy absorption prior to densification. Furthermore, the initial auxetic response is primarily associated with the rotational deformation of the inclined walls, whereas the subsequent plateau stage is governed by progressive plastic hinge formation, internal load redistribution, and coordinated collapse among neighboring cells. In the REDA structure,

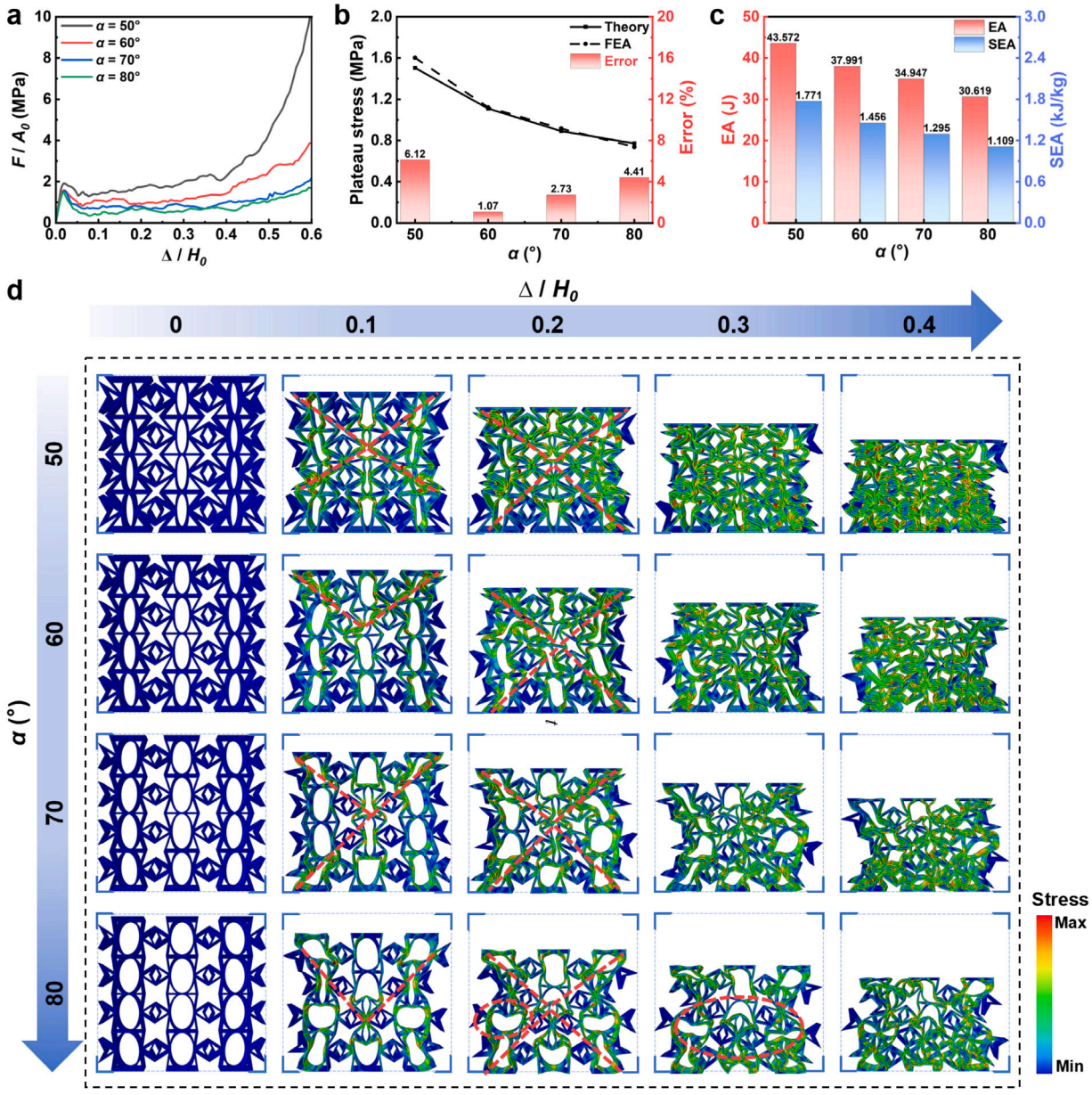

Fig. 6. Comparison of energy absorption under different α values. a. Stress–strain curves for different values of α; **b.** Effect of varying α on plateau stress; **c.** Effect of varying α on EA and SEA; **d.** Finite element results under quasi-static compression for different values of α.

the elliptical and double-arrow reinforcements help sustain this coordinated deformation over a broader strain range, thereby improving both auxetic stability and energy absorption efficiency.

The corresponding energy absorption performance of the different structures under quasi-static compression at the same relative density is shown in Fig. 5c. Compared with RHC, RH, SRH, and EARE, the REDA structure exhibited significantly enhanced mechanical performance. Specifically, the plateau stress of REDA increased by 81.98%, 60.60%, 62.92%, and 18.88%, respectively, while the SEA increased by 202.07%, 138.30%, 67.16%, and 52.14%, respectively, demonstrating the superior energy absorption capability of the REDA structure among the compared configurations.

3.3. Parametric studies

Since quasi-static compression is widely representative in engineering, understanding the influence of geometric parameters on mechanical performance is essential for structural optimization and prediction [62]. In the present study, the developed theoretical model incorporates the coupled influence of the key geometric parameters through the derived plateau stress formulation. The re-entrant angle α, the double-arrow angles β and γ, and the strut thickness t collectively affect the deformation behavior, load-transfer paths, and plastic energy dissipation of the REDA structure. Based on this, the parametric study focuses on these representative geometric variables and analyzes their influence on the EA, SEA, and plateau stress of the REDA structure within practical parameter ranges. For the experimental and numerical parametric analyses, a controlled-variable strategy is adopted, in which only one parameter is varied at a time while the remaining parameters are kept constant, so as to clearly reveal the dominant mechanical trends associated with each geometric variable.

3.3.1. Effect of α

Four REDA structures with different unit cell angles α were obtained by keeping $\beta = 60°$, $\gamma = 30°$, $t = 0.8$ mm, $l = 10$ mm, and $w = 18$ mm constant, and increasing α from 50° to 80° in increments of 10°. As shown in Fig. 6a, finite element stress–strain curves indicate that

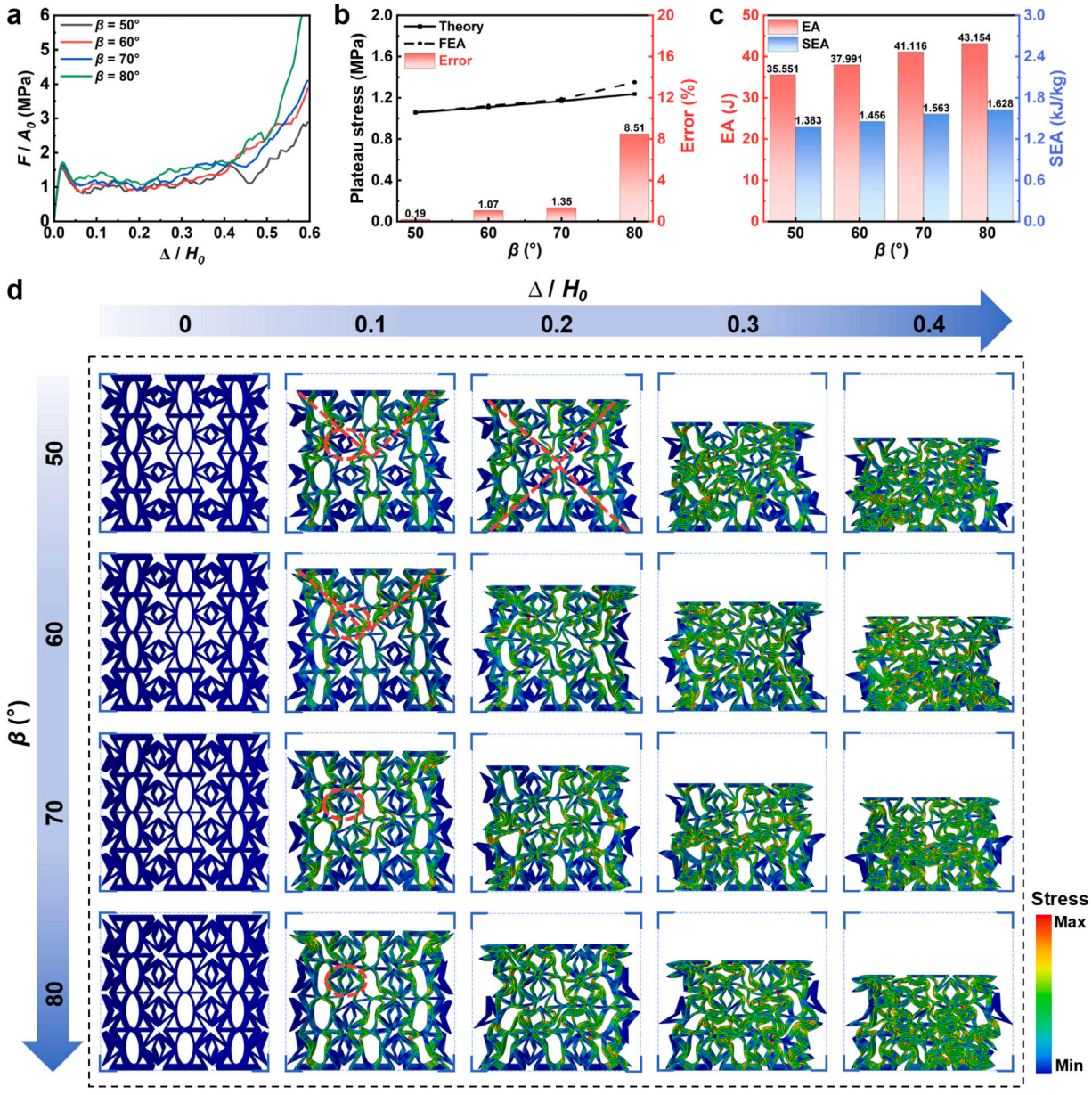

Fig. 7. Comparison of energy absorption under different β values. a. Stress–strain curves for different values of β; **b.** Effect of varying β on plateau stress; **c.** Effect of varying β on EA and SEA; **d.** Finite element results under quasi-static compression for different values of β.

overall stress decreases with increasing α. Fig. 6b shows good agreement between theoretical and FEA plateau stresses, with relative errors mostly within 5%, and a clear decreasing trend as α increases. This occurs because smaller α allows earlier and fuller engagement of the double-arrow connections, effectively suppressing local buckling and forming more plastic hinges, whereas larger α delays force transmission and reduces structural stability. As shown in Fig. 6c, EA and SEA follow a similar trend, decreasing with larger α because smaller angles produce elongated ellipses that enhance connectivity, while larger angles yield more rounded ellipses with weaker support.

As shown in Fig. 6d, REDA deformation modes vary with α under quasi-static compression. At 10% strain, all structures exhibit relatively uniform local buckling. As α increases, elliptical units become more rounded, dispersing buckling in the middle region. At 20% strain, the V-shaped buckling band propagates toward both ends, with smaller α producing concentrated bands and larger α forming clearer continuous paths. Excessively large α causes premature instability. By 30% strain, smaller α maintains uniform collapse, while larger α leads to local instability and overall non-uniform collapse of the structure, as indicated by the regions circled with red ellipses in Fig. 6d, where localized deformation concentration and premature inward collapse can be observed. All structures reach densification at 40% strain. Overall, increasing α shifts deformation from uniform collapse to concentrated abrupt failure, reducing energy absorption and compression stability.

3.3.2. *Effect of β*

Four REDA structures with different unit cell angles β were obtained by keeping $\alpha = 60°$, $\gamma = 30°$, $t = 0.8$ mm, $l = 10$ mm, and $w = 18$ mm constant, while β was increased from 50° to 80° in increments of 10°. Fig. 7a shows finite element stress–strain curves for different β values. As β increases, stress slightly rises in the plastic and densification stages, indicating modestly improved compressive capacity. Fig. 7b shows good agreement between theoretical and FEA plateau stresses, with relative errors within 5%. Plateau stress moderately rises with larger β as the long edges of the double-arrow units engage the re-entrant inclined edges earlier, allowing more continuous load-bearing

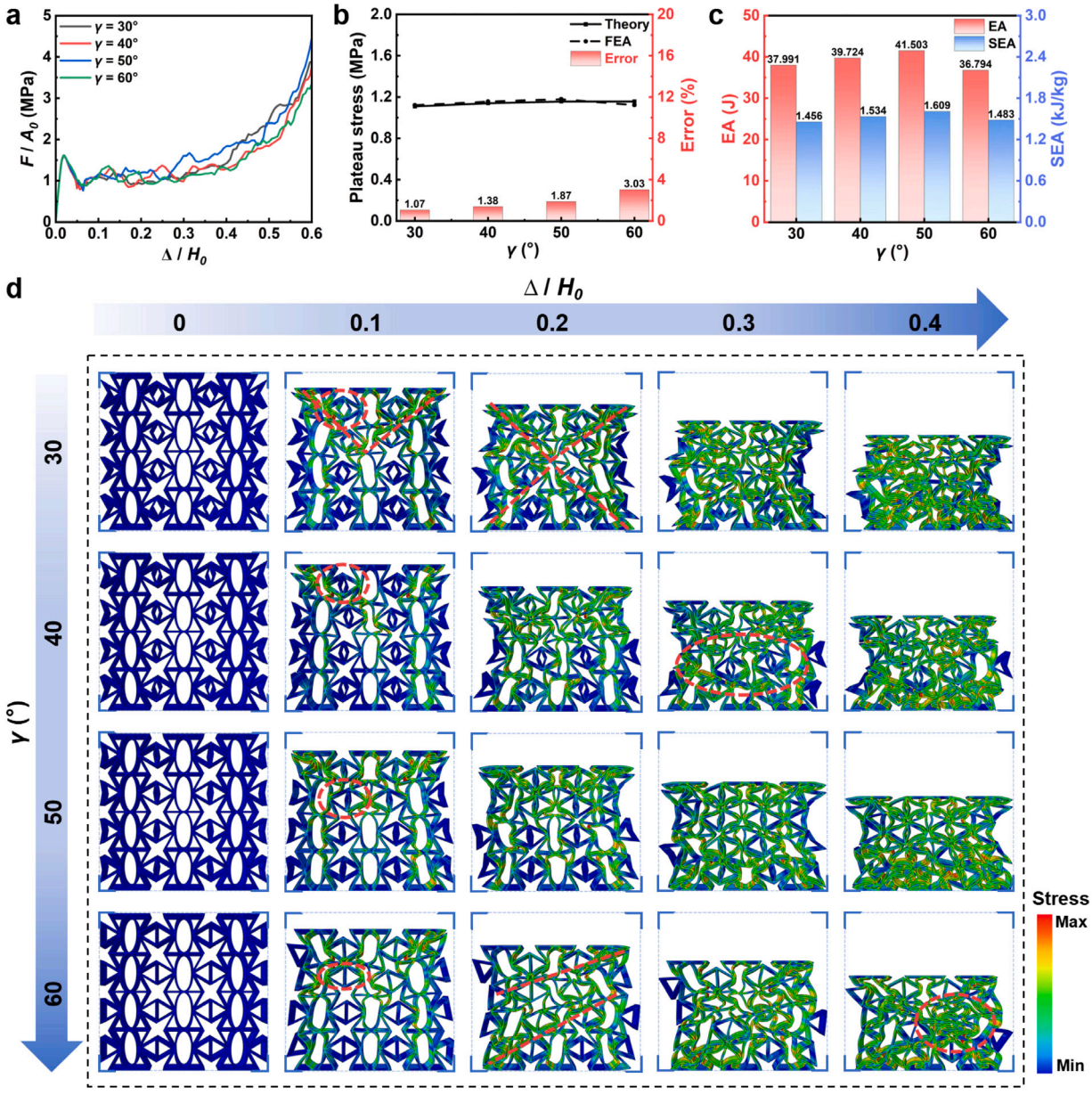

Fig. 8. Comparison of energy absorption under different γ values. a. Stress–strain curves for different values of γ; **b.** Effect of varying γ on plateau stress; **c.** Effect of varying γ on EA and SEA; **d.** Finite element results under quasi-static compression for different values of γ.

in the plastic phase. EA and SEA show a similar slight upward trend, as shown in Fig. 7c. Overall, changes are minor, since deformation is mainly governed by the re-entrant honeycomb and elliptical units, with double-arrow units primarily affecting load transfer timing.

Fig. 7d shows finite element deformation modes during quasi-static compression for different β values. At 10% strain, all structures show V-shaped buckling in the upper region. Larger β reduces the initial angle between the double-arrow long edge and re-entrant inclined edge, allowing earlier engagement and more pronounced V-shaped bands. At 20% strain, V-shaped bands also appear in the lower region. Small β maintains uniform, stable buckling paths, while larger β causes broader contact, concentrated local collapse, rapid pore shrinkage, and uneven folding. By 30% strain, larger β produces irregular folding with extensive double-arrow deformation, and by 40% all structures reach densification. Overall, increasing β advances buckling and slightly improves energy absorption, while the re-entrant honeycomb and elliptical units remain the main contributors.

3.3.3. *Effect of* γ

Four REDA structures with different unit cell angles γ were obtained by keeping $\alpha = 60°$, $\beta = 60°$, $t = 0.8$ mm, $l = 10$ mm, and $w = 18$ mm constant, while γ was increased from 30° to 60° in increments of 10°. Fig. 8a shows finite element stress–strain curves for different γ values. As γ increases, stress initially rises and then decreases. Small γ yields low, smooth curves, while larger γ increases stress but introduces fluctuations, indicating enhanced yet less stable load-bearing. At $\gamma = 60°$, the curve drops as the two short sides of the double-arrow unit merge into a single vertical edge, reducing load paths and transfer efficiency. Fig. 8b shows good agreement between theoretical and FEA plateau stresses, with most relative errors within 5%. Overall, plateau stress generally rises with γ, since larger angles require greater rotation of the double-arrow units to sustain energy absorption during the plastic stage, though $\gamma = 60°$ slightly reduces it. As shown in Fig. 8c, EA and SEA follow a similar trend. Overall changes are minor because energy absorption is mainly governed by the re-entrant honeycomb and

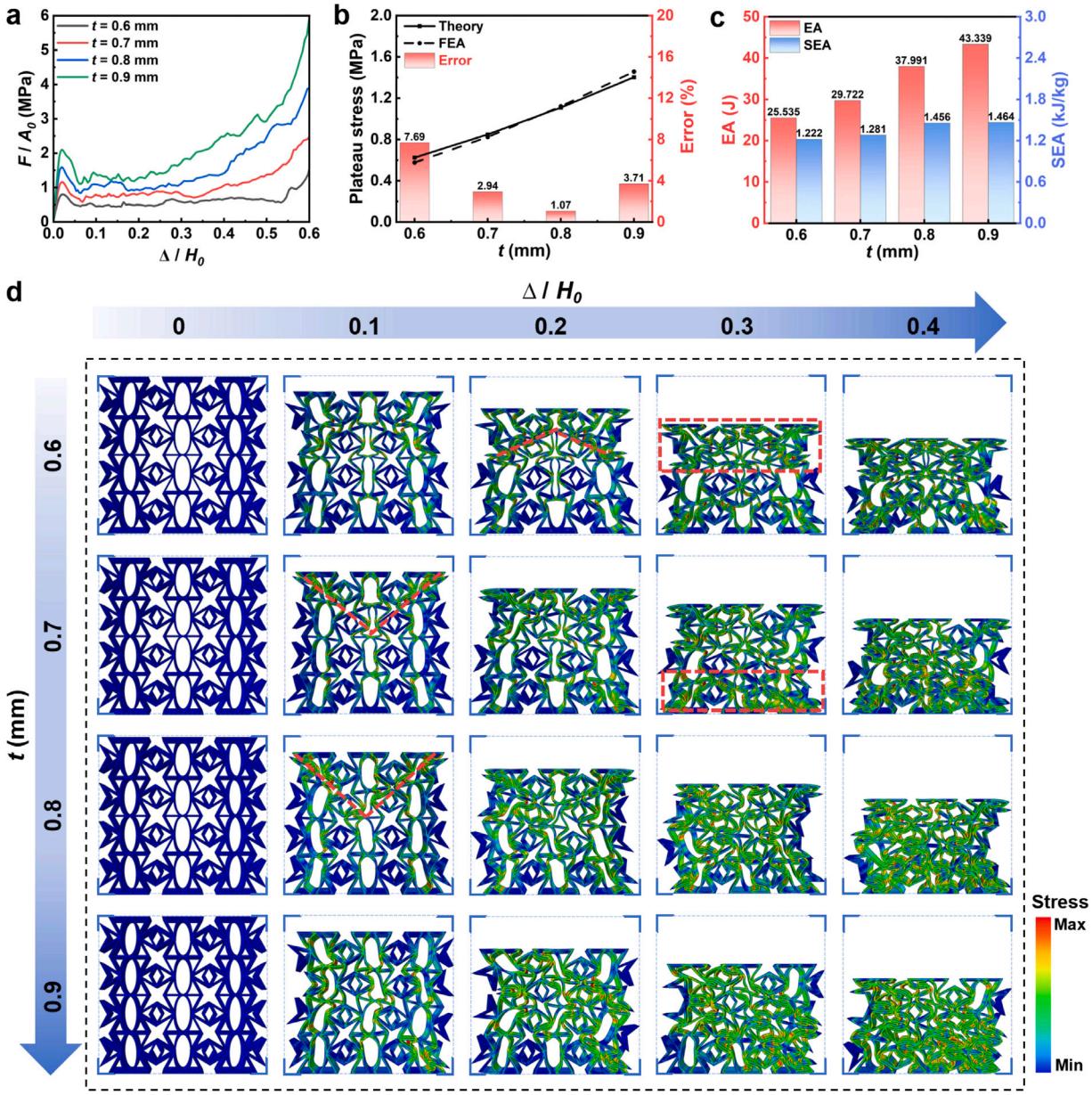

Fig. 9. Comparison of energy absorption under different t values. a. Stress–strain curves for different values of t; **b.** Effect of varying t on plateau stress; **c.** Effect of varying t on EA and SEA; **d.** Finite element results under quasi-static compression for different values of t.

elliptical units, while variations in the double-arrow units mainly serve to prolong deformation.

Fig. 8d shows the finite element deformation modes under different γ values during quasi-static compression. At 10% strain, all structures exhibit central V-shaped buckling bands. With increasing γ, the short edges of the double-arrow units become more vertical, delaying load-bearing engagement and promoting more concentrated and less continuous buckling. At 20% and 30% strain, smaller γ values maintain progressive and continuous collapse with relatively intact pores, whereas larger γ values exhibit pronounced diagonal collapse, irregular local buckling, and concentrated deformation. At 40% strain, all structures approach densification, with smaller γ showing more uniform compaction and larger γ displaying localized collapse. Overall, increasing γ shifts the deformation mode from uniform and stable to concentrated and irregular, with $\gamma = 60°$ inducing a distinct instability due to the merging of the short edges into a single vertical edge.

3.3.4. *Effect of t*

Four REDA structures with different unit cell thicknesses t were modeled by increasing t from 0.6 mm to 0.9 mm in 0.1 mm increments, while keeping $\alpha = 60°$, $\beta = 60°$, $\gamma = 30°$, $l = 10$ mm, and $w = 18$ mm constant. Fig. 9a shows the stress–strain curves under quasi-static compression, indicating that increasing t raises the overall stress level. As shown in Fig. 9b, the theoretically predicted plateau stresses agree well with the finite element results and increase monotonically with increasing t. Especially at large strains, because the thicker cell walls exhibit higher bending stiffness due to the increased inertia of the cell wall cross-section. Correspondingly, Fig. 9c shows that both EA and SEA increase with thickness, as the enhanced bending stiffness and load-bearing capacity allow the structure to sustain higher stresses and absorb more energy during compression.

Fig. 9d shows the deformation modes under different thicknesses t during quasi-static compression. At 10% strain, structures with small t develop large V-shaped buckling bands with deformation localized in

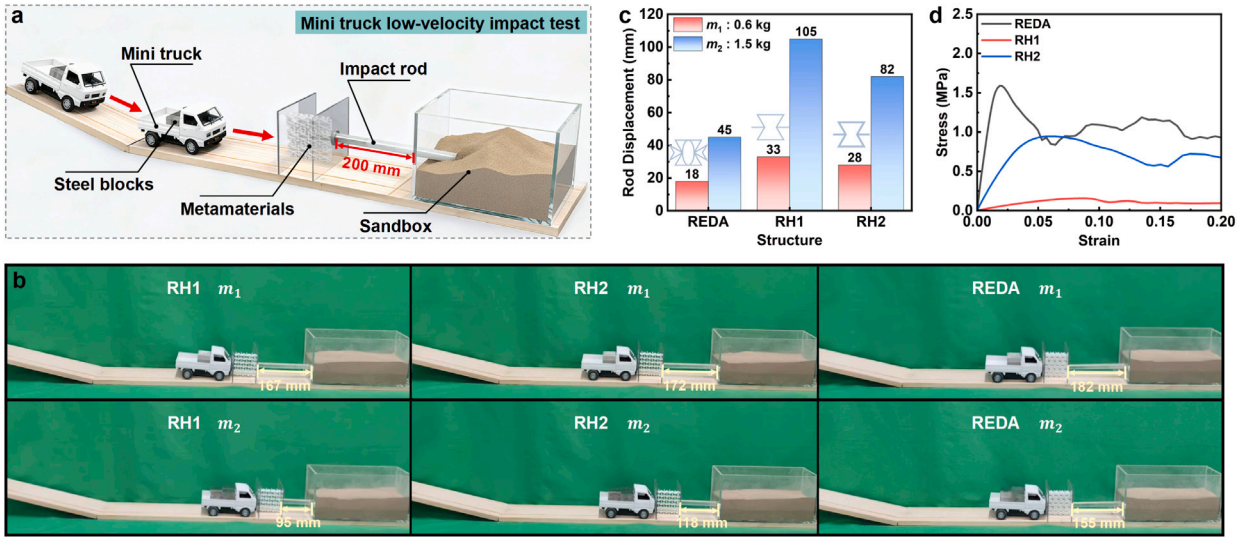

Fig. 10. Experimental evaluation of the protective performance of mechanical metastructures. a. Sandbox collision experimental setup of mini truck; **b.** Comparison of different test cases after mini truck collision; **c.** Cushioning performance of mechanical metastructures under impact tests; **d.** Stress–strain responses of mechanical metastructures under quasi-static compression.

unstable regions, whereas increasing t leads to more localized buckling and broader load-bearing participation. At 20% strain, small t causes severe cell instability and large bending, while larger t promotes progressive local bending with a stable global profile. By 30% strain, small t results in rapid, layered collapse due to the spread of large-amplitude instability, whereas larger t produces more uniform collapse with distributed buckling bands. At 40% strain, all structures approach densification, with small t dominated by large bending and intercell contact, and larger t exhibiting controlled, layer-by-layer buckling. Overall, increasing t enhances cell-wall bending stiffness and load-bearing capacity, suppresses large-scale instability, and improves deformation uniformity, structural stability, and energy absorption.

4. Application demonstration for mini truck

To further evaluate the protective performance of the proposed REDA structure under practical impact conditions, a laboratory-scale mini truck low-velocity impact test was conducted to assess its energy absorption capability under dynamic loading. A simplified measurement setup was developed to address the challenges of quantifying damage from low-velocity impacts, which are characterized by short durations and subtle effects. As shown in Fig. 10a, the setup consists of four main components: a sand box, an impact rod, a protective unit made of the REDA structure, and the mini truck body. The sand box was filled with fine sand. One end of the impact rod was inserted into the sand to measure the penetration depth as a proxy for the transmitted force, while the other end contacted the REDA specimen. During the test, the mini truck slid freely down a wooden ramp with a height of 0.25 m and a length of 1 m. This sliding motion would ideally result in an impact velocity of approximately 2.2 m/s, neglecting friction and other energy losses. The entire collision process was recorded and is provided in the supplementary video. To investigate the protective performance under different impact energies, the total mini truck mass was adjusted to 0.6 kg and 1.5 kg by adding steel blocks. The ramp height and length were kept constant, ensuring identical initial conditions before impact.

In the mini truck low-velocity impact experiments, the penetration depth of the impact rod is employed as an indirect quantitative indicator of the residual impact energy transmitted through the protective structure. The principle of this experimental approach is based on the transfer and dissipation of impact energy during collision. During the impact process, the kinetic energy of the mini truck is partially absorbed by the REDA structure through elastic bending, progressive buckling, localized deformation of the struts, and coordinated deformation interactions among adjacent unit cells. The remaining energy is subsequently transmitted to the impact rod, which penetrates into the granular medium in the sand box. During this process, energy is further dissipated through frictional resistance, particle rearrangement, compaction, and local deformation within the sand medium. Therefore, the insertion depth of the rod reflects the amount of residual energy transmitted through the structure. A smaller penetration depth indicates that a larger proportion of the impact energy has been absorbed by the structure, corresponding to better cushioning and protective performance, whereas a larger penetration depth indicates lower energy absorption efficiency. The penetration depth does not represent a direct measurement of stress or force, but serves as a comparative indicator of transmitted impact energy under identical experimental conditions. By maintaining consistent impact conditions throughout the tests, the penetration depth provides a practical and repeatable metric for evaluating the relative impact attenuation capability of different structures under low-velocity impact conditions.

Fig. 10b shows the impact-test results for the different structures under the two mass conditions. To comprehensively evaluate the protective performance of the REDA structure, two representative re-entrant honeycomb structures, designated RH1 and RH2, were selected for comparison. The RH1 structure has the same unit size as the REDA structure, which allows an analysis of how differences in geometric configuration affect energy absorption performance. In contrast, the RH2 structure was designed to have the same relative density as the REDA structure, enabling a comparison of protective efficiency between different structural forms under equal material utilization. To ensure reliability, each structural configuration was tested three times under each mass condition, and the measured penetration depths showed good consistency across repeated tests, indicating satisfactory experimental repeatability. Potential experimental uncertainties may originate from geometric deviations introduced during the FDM printing process, local thin-wall regions, micro-voids, interlayer bonding defects, and slight impact alignment deviations during collision. These effects were minimized by maintaining consistent fabrication parameters and testing conditions for all specimens.

As shown in Fig. 10c, the penetration depths differed significantly among the structures under identical impact conditions. The REDA structure exhibited the smallest penetration depths in both mass cases, with values of only 18 mm at 0.6 kg and 45 mm at 1.5 kg. These values

are substantially lower than the 33 mm and 105 mm measured for the RH1 structure, and also lower than the 28 mm and 82 mm measured for the RH2 structure under the respective mass conditions. Compared to RH1, REDA reduced penetration depth by approximately 45.5% under the low-mass condition and 57.1% under the high-mass condition. The corresponding reductions compared to RH2 were 35.7% and 45.1%. These results clearly demonstrate that the REDA structure can significantly attenuate the transmitted impact load across different energy levels, confirming its superior energy absorption capacity and protective stability. A comparative analysis of the growth rates reveals that as impact energy increases, the penetration depth rises substantially for all three structures. The RH1 and RH2 structures showed growth rates of 218% and 193%, respectively, while the REDA structure shows only a 150% increase. Moreover, its absolute displacement remains the lowest among the three, indicating that the REDA structure can continuously absorb more energy under higher impact energies, thereby effectively reducing the transmitted impact load to the rear end.

These results indicate that the REDA structure provides enhanced load attenuation and structural stability across different impact energy levels. This macroscopic response is consistent with the stress–strain behavior presented in Fig. 10d. Within the small- to moderate-strain regime corresponding to the deformation range achieved in the low-velocity impact demonstration, the REDA structure maintains a substantially higher stress level than RH1 and RH2. As energy absorption is proportional to the area under the stress–strain curve, the larger integral of REDA in this strain interval implies greater energy absorption even without entering a fully developed crushing stage. The superior impact attenuation capability of the REDA structure can be attributed to its enhanced initial stiffness and more coordinated deformation behavior. The enhanced initial modulus enables rapid stress buildup during early deformation, allowing more elastic energy to be stored at small strains. Meanwhile, the relatively higher stress plateau facilitates early-stage plastic dissipation before global instability occurs. Consequently, energy is dissipated through controlled and distributed deformation rather than through abrupt structural collapse. Overall, these results highlight the dynamic response of the REDA structure under different impact conditions and demonstrate its superior performance compared with conventional re-entrant honeycomb structures. The REDA configuration consistently exhibits lower penetration depths and higher stress levels, indicating enhanced load attenuation, improved energy absorption, and greater structural stability across varying impact energies.

However, in the mini truck low-velocity impact tests, the REDA structure did not undergo complete failure. Only part of the impactor's kinetic energy was absorbed by the structure, while a significant portion was dissipated through interaction between the impact rod and the sand in the container, including friction and granular rearrangement. The short duration of the impact and the distributed nature of the contact force further reduced the likelihood of global structural failure, resulting in relatively small deformation. These observations demonstrate the REDA structure's capability for load attenuation and momentum buffering under different impact conditions, reflecting its ability to moderate transmitted loads during low-velocity impacts. Accordingly, the present results should be interpreted as supportive evidence of enhanced impact attenuation capability under low-velocity conditions rather than as a comprehensive quantitative assessment of dynamic crushing behavior.

In summary, compared with conventional re-entrant structures, REDA provides enhanced protective performance, highlighting its potential for applications in vehicle crashworthiness, vibration mitigation, and engineering protective systems.

5. Conclusions and future works

This study proposes a novel re-entrant elliptical double-arrow hybrid honeycomb that integrates arrowhead connections and internal elliptical supports to enhance load transfer and buckling resistance. Theoretical analysis, numerical simulations, and experiments consistently demonstrate its excellent stability and energy absorption performance. Compared with conventional re-entrant honeycombs, REDA exhibits significantly improved specific energy absorption. The proposed theoretical model accurately predicts the plateau stress, showing good agreement with simulations. Parametric studies and mini truck impact tests further confirm its controllable deformation and superior load mitigation, highlighting its strong potential for lightweight energy-absorbing and protective applications.

However, the present work primarily focuses on quasi-static compression behavior and single-material PLA specimens under relatively low-velocity impact conditions, with a limited number of unit cells considered in the numerical models. Therefore, the mechanical response of the REDA structure under dynamic loading and larger-scale configurations still requires further investigation. Future work will focus on high-strain-rate impact behavior, strain-rate-sensitive constitutive characterization, repeated impact resistance, and dynamic failure mechanisms, together with larger-scale periodic models and different material systems, including metallic and composite structures. More advanced constitutive formulations incorporating strain-rate sensitivity, damage evolution, and anisotropic effects will also be considered to further evaluate the crashworthiness and practical engineering applicability of the proposed structure under realistic service conditions.

In addition, PLA was selected in this study primarily because of its excellent printability, dimensional stability, and compatibility with FDM fabrication, which facilitates the reliable manufacturing and experimental validation of complex thin-walled auxetic structures. The present work mainly focuses on validating the proposed geometry-driven design concept and its deformation and energy absorption mechanisms under quasi-static compression. Although PLA exhibits lower stiffness and impact resistance than metallic or composite materials, the enhancement mechanism of the REDA structure mainly originates from the synergistic interaction between the elliptical reinforcement units and the double-arrow load-transfer paths, and is therefore expected to remain effective across different material systems. If fabricated using metallic or fiber-reinforced composite materials, the REDA structure may achieve improved load-bearing capacity, specific energy absorption, and crashworthiness performance, although the associated deformation and failure mechanisms may differ due to material-dependent behaviors. Future work will further investigate REDA structures fabricated using metallic and composite materials under dynamic and repeated impact conditions.

Furthermore, the present numerical models employ a limited number of unit cells along the main in-plane directions to ensure computational efficiency and consistent comparison among different honeycomb configurations. However, such finite-size models may introduce boundary effects and may not fully represent the bulk mechanical properties of large-scale periodic cellular structures. Increasing the number of unit cells may improve deformation coordination and reduce boundary-induced stress concentration, which may influence the plateau stress, energy absorption evolution, and deformation localization behavior of the structure. In addition, the influence of directional-dependent mechanical anisotropy under different in-plane loading orientations also requires further investigation. Therefore, future work will establish larger-scale periodic numerical models to evaluate the bulk mechanical response of the REDA structure and reduce the influence of boundary constraints.

Finally, future work will establish a more comprehensive multi-parameter optimization framework to investigate the nonlinear coupling effects among geometric variables and to further optimize the balance between stiffness, deformation stability, auxeticity, and energy absorption performance of the REDA structure.

CRediT authorship contribution statement

Wenpeng Xu: Writing – original draft, Validation, Supervision, Resources, Project administration, Methodology, Investigation, Funding acquisition, Formal analysis, Conceptualization. **Dongxia Wang:** Writing – review & editing, Writing – original draft, Visualization, Validation, Methodology, Investigation, Formal analysis, Data curation. **Jinglong Zhang:** Validation, Investigation, Formal analysis. **Jiahe Hu:** Validation, Investigation. **Hao Xu:** Writing – review & editing, Writing – original draft, Validation, Project administration, Methodology, Investigation, Formal analysis, Data curation, Conceptualization. **Liuchao Jin:** Writing – review & editing, Writing – original draft, Visualization, Validation, Project administration, Methodology, Investigation, Formal analysis, Data curation, Conceptualization. **Haitao Ye:** Validation, Methodology, Investigation, Formal analysis. **Haisen Zhao:** Validation, Methodology, Investigation, Formal analysis. **Wei-Hsin Liao:** Writing – review & editing, Validation, Supervision, Resources, Project administration, Investigation, Funding acquisition.

Declaration of competing interest

The authors declare that they have no known competing financial interests or personal relationships that could have appeared to influence the work reported in this paper.

Acknowledgments

Wenpeng Xu acknowledges the support by the Natural Science Foundation of Henan Province, China (No. 242300420281 and No. 252300421511) and the Fundamental Research Funds for the Universities of Henan Province (No. NSFRF240817). Liuchao Jin acknowledges the support by the Hong Kong Research Grants Council under the Hong Kong PhD Fellowship Scheme (No. PF21-60853). Haisen Zhao acknowledges the support by the National Natural Science Foundation of China (Grant Nos. U23A20312 and 62472257). Wei-Hsin Liao acknowledges the support by Hong Kong Research Grants Council (C4074-22G and STG5/E-103/24-R), and The Chinese University of Hong Kong (Project ID: 3110174).

Appendix A. Supplementary data

Supplementary material related to this article can be found online at https://doi.org/10.1016/j.tws.2026.115252.

Data availability

The data that support the findings of this study are openly available in figshare at: https://doi.org/10.6084/m9.figshare.31725139.

References

[1] Q. Gao, X. Ni, R. Liu, H. Luo, J. Zhou, Y. Su, Y. Tang, F. Dong, X. Wang, W.-H. Liao, Auxetic structures for energy absorption: A review on design, manufacturing, optimization, and applications, J. Intell. Mater. Syst. Struct. 37 (5) (2026) 263–301.

[2] N. Abdullah, M. Sani, M. Salwani, N. Husain, A review on crashworthiness studies of crash box structure, Thin-Walled Struct. 153 (2020) 106795.

[3] R. Yao, Y. Wei, B. Zhang, E. Wang, X. Yang, Q. Li, G. Sun, Lightweight design and passive safety innovations in transportation, Thin-Walled Struct. (2026) 114753.

[4] Y. Chen, Potential auxetic honeycomb system constructed from a new re-entrant block, Eng. Struct. 340 (2025) 120718.

[5] E. Wang, R. Yao, Q. Li, X. Hu, G. Sun, Lightweight metallic cellular materials: a systematic review on mechanical characteristics and engineering applications, Int. J. Mech. Sci. 270 (2024) 108795.

[6] S. Ouyang, W. Li, H. Poh Leong, Y. Zhong, Y. Tang, Dual-enhanced stiffness and auxeticity in novel double re-entrant honeycombs with vertical fold-line stiffeners, Thin-Walled Struct. 217 (2025) 113746.

[7] Q. Gao, C. Ge, W. Zhuang, L. Wang, Z. Ma, Crashworthiness analysis of double-arrowed auxetic structure under axial impact loading, Mater. Des. 161 (2019) 22–34.

[8] Z. Cui, J. Zhao, R. Xu, Y. Ding, Z. Sun, Mechanical design and energy absorption performances of novel plate-rod hybrid lattice structures, Thin-Walled Struct. 194 (2024) 111349.

[9] R. Li, Y. Zhong, Y. Tang, R. Liu, Enhanced specific stiffness and energy absorption in star-re-entrant hierarchical honeycombs featuring two plateau stages, Thin-Walled Struct. 211 (2025) 113050.

[10] G. Sun, D. Chen, G. Zhu, Q. Li, Lightweight hybrid materials and structures for energy absorption: A state-of-the-art review and outlook, Thin-Walled Struct. 172 (2022) 108760.

[11] Y. Wu, J. Fang, C. Wu, C. Li, G. Sun, Q. Li, Additively manufactured materials and structures: A state-of-the-art review on their mechanical characteristics and energy absorption, Int. J. Mech. Sci. 246 (2023) 108102.

[12] W. Li, Y. Zhong, Y. Zhu, H. Cao, R. Liu, Enhancing the structural stiffness and energy absorption of re-entrant auxetic honeycombs using folded stiffeners, Thin-Walled Struct. 205 (2024) 112504.

[13] Q. Gao, L. Wang, Z. Zhou, Z. Ma, C. Wang, Y. Wang, Theoretical, numerical and experimental analysis of three-dimensional double-v honeycomb, Mater. Des. 139 (2018) 380–391.

[14] Q. Gao, W.-H. Liao, L. Wang, An analytical model of cylindrical double-arrowed honeycomb with negative Poisson's ratio, Int. J. Mech. Sci. 173 (2020) 105400.

[15] X. Yang, J. Ma, D. Wen, J. Yang, Crashworthy design and energy absorption mechanisms for helicopter structures: A systematic literature review, Prog. Aerosp. Sci. 114 (2020) 100618.

[16] L. Hu, M.Z. Zhou, H. Deng, Dynamic indentation of auxetic and non-auxetic honeycombs under large deformation, Compos. Struct. 207 (2019) 323–330.

[17] S. Huang, Y. Liu, K. Wen, X. Su, C. Liang, H. Duan, G. Zhao, Optimization design of a novel microwave absorbing honeycomb sandwich structure filled with magnetic shear-stiffening gel, Compos. Sci. Technol. 232 (2023) 109883.

[18] Y. Duan, Z. Liu, X. Zhao, N. Hou, B. Du, H. Liu, Z. Zhao, B. Hou, Y. Li, L.N. Rabinskiy, Crushing behavior of honeycomb vs. foam under combined shear-compression loading, Int. J. Impact Eng. 146 (2020) 103696.

[19] P. Kumar, L. Kucherov, M. Ryvkin, Fracture toughness of self-similar hierarchical material, Int. J. Solids Struct. 203 (2020) 210–223.

[20] G. Sun, X. Huo, H. Wang, P.J. Hazell, Q. Li, On the structural parameters of honeycomb-core sandwich panels against low-velocity impact, Compos. Part B: Eng. 216 (2021) 108881.

[21] X. Zhao, Q. Gao, L. Wang, Q. Yu, Z. Ma, Dynamic crushing of double-arrowed auxetic structure under impact loading, Mater. Des. 160 (2018) 527–537.

[22] G. Sun, D. Chen, H. Wang, P.J. Hazell, Q. Li, High-velocity impact behaviour of aluminium honeycomb sandwich panels with different structural configurations, Int. J. Impact Eng. 122 (2018) 119–136.

[23] Y. Tang, P.L. Hien, Z. Yifeng, L. Rong, Enhanced tensile performance and energy absorption in elliptic-profile re-entrant honeycombs, Int. J. Mech. Sci. 304 (2025) 110708.

[24] S. Zhou, K. Zhang, L. Jin, Q. Gao, W.-H. Liao, Efficient data driven optimization framework for designing B-spline honeycombs with excellent energy absorption, Thin-Walled Struct. 209 (2025) 112941.

[25] L. Jin, S. Yu, J. Cheng, H. Ye, X. Zhai, J. Jiang, K. Zhang, B. Jian, M. Bodaghi, Q. Ge, W.-H. Liao, Machine learning driven forward prediction and inverse design for 4D printed hierarchical architecture with arbitrary shapes, Appl. Mater. Today 40 (2024) 102373.

[26] L. Jin, S. Yu, J. Cheng, Z. Liu, K. Zhang, S. Zhou, X. He, G. Xie, M. Bodaghi, Q. Ge, W.-H. Liao, Machine learning powered inverse design for strain fields of hierarchical architectures, Compos. Part B: Eng. 299 (2025) 112372.

[27] L. Jin, K. Zhang, S. Zhou, G. Xie, W.-H. Liao, Modulus tunability in hierarchical architectures: a machine learning-enabled approach, in: Multifunctional Materials and Structures, vol. 13433, SPIE, 2025, pp. 133–143.

[28] L. Jin, X. Zhai, J. Jiang, K. Zhang, W.-H. Liao, Optimizing stimuli-based 4D printed structures: a paradigm shift in programmable material response, in: Sensors and Smart Structures Technologies for Civil, Mechanical, and Aerospace Systems 2024, vol. 12949, SPIE, 2024, pp. 321–332.

[29] Z.-X. Lu, X. Li, Z.-Y. Yang, F. Xie, Novel structure with negative Poisson's ratio and enhanced Young's modulus, Compos. Struct. 138 (2016) 243–252.

[30] M.-H. Fu, Y. Chen, L.-L. Hu, A novel auxetic honeycomb with enhanced in-plane stiffness and buckling strength, Compos. Struct. 160 (2017) 574–585.

[31] M.-H. Fu, Y. Chen, L.-L. Hu, Bilinear elastic characteristic of enhanced auxetic honeycombs, Compos. Struct. 175 (2017) 101–110.

[32] H. Ye, X. Huang, L. Jin, S. Zhou, G. Xie, Z. Hu, R. Li, H. Mo, S. Fang, W.-H. Liao, et al., Multi-material 3D printed compression-induced stretching lattice metamaterials with superior reusable energy absorption, Virtual Phys. Prototyp. 21 (1) (2026) e2637380.

[33] H. Jiang, Y. Ren, Q. Jin, G. Zhu, Y. Hu, F. Cheng, Crashworthiness of novel concentric auxetic reentrant honeycomb with negative Poisson's ratio biologically inspired by coconut palm, Thin-Walled Struct. 154 (2020) 106911.

[34] X. Zhang, J. Wang, Q. Sun, J. Li, S. Zhou, J. Qi, R. Tao, Mechanical design and analysis of bio-inspired reentrant negative Poisson's ratio metamaterials with rigid-flexible distinction, Int. J. Smart Nano Mater. 15 (1) (2024) 1–20.
[35] T. Baran, M. Öztürk, In-plane elasticity of a strengthened re-entrant honeycomb cell, Eur. J. Mech. A Solids 83 (2020) 104037.
[36] X.-C. Zhang, C.-C. An, Z.-F. Shen, H.-X. Wu, W.-G. Yang, J.-P. Bai, Dynamic crushing responses of bio-inspired re-entrant auxetic honeycombs under in-plane impact loading, Mater. Today Commun. 23 (2020) 100918.
[37] X.Y. Zhang, X. Ren, Y. Zhang, Y.M. Xie, A novel auxetic metamaterial with enhanced mechanical properties and tunable auxeticity, Thin-Walled Struct. 174 (2022) 109162.
[38] M.S. Tatlıer, M. Öztürk, T. Baran, Linear and non-linear in-plane behaviour of a modified re-entrant core cell, Eng. Struct. 234 (2021) 111984.
[39] D. Zhu, Y. Wei, X. Shen, K. Yan, M. Yuan, S. Qi, A novel elliptical annular re-entrant auxetic honeycomb with enhanced stiffness, Int. J. Mech. Sci. 262 (2024) 108732.
[40] Y. Chen, Z.-W. Wang, In-plane elasticity of the re-entrant auxetic hexagonal honeycomb with hollow-circle joint, Aerosp. Sci. Technol. 123 (2022) 107432.
[41] L. Li, F. Yang, S. Zhang, Z. Guo, L. Wang, X. Ren, M. Zhao, A novel hybrid auxetic honeycomb with enhanced load-bearing and energy absorption properties, Eng. Struct. 289 (2023) 116335.
[42] K. Mo, F. Lu, C. Zhang, Y. Liu, Y. He, T. Wei, Y. Zhu, Energy absorption characteristics of a novel hierarchical auxetic star-shaped honeycomb, Thin-Walled Struct. 215 (2025) 113598.
[43] C. Qi, F. Jiang, A. Remennikov, L.-Z. Pei, J. Liu, J.-S. Wang, X.-W. Liao, S. Yang, Quasi-static crushing behavior of novel re-entrant circular auxetic honeycombs, Compos. Part B: Eng. 197 (2020) 108117.
[44] C. Qi, F. Jiang, S. Yang, A. Remennikov, Multi-scale characterization of novel re-entrant circular auxetic honeycombs under quasi-static crushing, Thin-Walled Struct. 169 (2021) 108314.
[45] C. Qi, F. Jiang, S. Yang, A. Remennikov, S. Chen, C. Ding, Dynamic crushing response of novel re-entrant circular auxetic honeycombs: Numerical simulation and theoretical analysis, Aerosp. Sci. Technol. 124 (2022) 107548.
[46] Y. Zhou, Y. Pan, L. Chen, Q. Gao, B. Sun, Mechanical behaviors of a novel auxetic honeycomb characterized by re-entrant combined-wall hierarchical substructures, Mater. Res. Express 9 (11) (2022) 115802.
[47] A. Alomarah, Y. Yuan, D. Ruan, A bio-inspired auxetic metamaterial with two plateau regimes: compressive properties and energy absorption, Thin-Walled Struct. 192 (2023) 111175.
[48] A. Alomarah, H.K. Dalfi, C. Rodrigo, D. Ruan, Compressive performances of 3D-bio-inspired auxetic metamaterials: Design and experiments, Thin-Walled Struct. 220 (2025) 114355.
[49] Z. Xu, Y. Cui, K. Wang, B. Wang, B. Wang, Quasi-static compression and impact resistances of novel re-entrant chiral hybrid honeycomb structures, Compos. Struct. 366 (2025) 119206.
[50] A. Alomarah, A.T. Abbas, B. Faisal, Z. Peng, D. Ruan, The effects of manufacturing techniques on the mechanical performance of an auxetic structure manufactured by fused filament fabrication and multijet fusion processes, Adv. Eng. Mater. 26 (7) (2024) 2302033.
[51] R. Yao, B. Zhang, Q. Niu, Q. Li, G. Sun, On modeling of extruded thin-walled multi-cell structures incorporating anisotropy yielding, strain hardening and damage failure, Thin-Walled Struct. 216 (2025) 113548.
[52] L. Wan, D. Hu, H. Zhang, Z. Yang, Energy absorption of foam-filled TPMS-based tubular lattice structures subjected to quasi-static lateral crushing, Eng. Struct. 316 (2024) 118581.
[53] X. Li, Z. Li, Z. Guo, Z. Guo, Z. Mo, J. Li, A novel hybrid star honeycomb with individually adjustable second plateau stresses, Compos. Struct. 356 (2025) 118881.
[54] F. Jiang, S. Yang, C. Ding, C. Qi, Quasi-static crushing behavior of novel circular double arrowed auxetic honeycombs: Experimental test and numerical simulation, Thin-Walled Struct. 177 (2022) 109434.
[55] A. Ingrole, A. Hao, R. Liang, Design and modeling of auxetic and hybrid honeycomb structures for in-plane property enhancement, Mater. Des. 117 (2017) 72–83.
[56] Q. Gao, W.-H. Liao, Energy absorption of thin walled tube filled with gradient auxetic structures-theory and simulation, Int. J. Mech. Sci. 201 (2021) 106475.
[57] H. Lu, X. Wang, T. Chen, In-plane dynamics crushing of a combined auxetic honeycomb with negative Poisson's ratio and enhanced energy absorption, Thin-Walled Struct. 160 (2021) 107366.
[58] C. Zhang, F. Lu, T. Wei, Y. Huang, Y. He, Y. Zhu, A novel windmill-shaped auxetic structure with energy absorption enhancement, Int. J. Mech. Sci. 280 (2024) 109635.
[59] Y. Zhu, Y. Fu, X. Rui, C. He, Q. Wang, C. Zhang, On the design and crashworthiness of a novel auxetic self-locking energy absorption system, Int. J. Solids Struct. 311 (2025) 113246.
[60] W. Wen, M. Lei, Y. Tao, Y. Lian, Out-of-plane crashworthiness of bio-inspired hierarchical diamond honeycombs with variable cell wall thickness, Thin-Walled Struct. 176 (2022) 109347.
[61] A. Esmaeili, M. Karimi, M. Heidari-Rarani, M. Shojaie, A new design of star auxetic metastructure with enhanced energy-absorption under various loading rates: experimental and numerical study, in: Structures, Structures vol. 63 (2024) 106457.
[62] P. Li, S. Chu, S. Qin, H. Ding, N. Luo, Y. Yu, T. Zhang, G. Xiong, Optimisation of prestressed stayed steel columns based on strengthen elitist genetic algorithm, J. Constr. Steel Res. 227 (2025) 109324.